

# Photoacoustic Imaging Sensors Based on Integrated Photonics: Challenges and Trends

Kangjian Bao, Xi Yang, Chunlei Sun, Guoguang Rong, Chao Tian, Junhui Shi, Mohamad Sawan,\* and Lan Li\*

Ultrasound and photoacoustic imaging are important imaging modalities with significant applications in clinical diagnosis and biomedical research. However, current capacitive and piezoelectric ultrasound detectors face challenges related to sensitivity and bandwidth, particularly at higher frequencies. These challenges can hinder their ability to achieve high spatial resolution and deep penetration for imaging purposes. Optical ultrasound sensors offer high sensitivity and show great potential for developing ultrasound/photoacoustic imaging systems. Among all methods of optical ultrasound detection, integrated photonics, with its superior advantages in miniaturization, sensitivity, and integration capability with electronics, could be next-generation photoacoustic/ultrasound imaging technology. This review explores the device structure designs and applications of ultrasound/photoacoustic sensing based on integrated photonics, analyzes their performance metrics as ultrasound detectors, and discusses some perspectives on future developments and trends in this field.

of pulse lasers, the theories of this phenomenon were further developed<sup>[2]</sup> by Askar'yan<sup>[3]</sup> (1963), White<sup>[4]</sup> (1963), Carome<sup>[5]</sup> (1964), Cleary<sup>[6]</sup> (1968), Burmistrova<sup>[7]</sup> (1978), and Karabutov<sup>[8,9]</sup> (1979 and 1985). Photoacoustic imaging (PAI) is an advanced technique that detects and visualizes acoustic waves produced by laser light absorption in biological tissues. By combining ultrasound with laser-induced signals, PAI offers a highly sensitive way to quickly image and differentiate optical absorption properties at various spatial scales.<sup>[10]</sup> Sub-micro level resolution can be effectively obtained in PAI when combined with optical microscopy techniques over superficial imaging.<sup>[11]</sup> And it allows for imaging at greater tissue depths as it experiences two orders of magnitude less ultrasonic scattering than optical

scattering.<sup>[12]</sup> By employing image reconstruction algorithms, obtaining a 3D image of objects, even in vivo, becomes possible. Moreover, the non-invasive nature of PAI minimizes harm to human bodies, making it highly suitable for biomedical research and clinical diagnosis.

The ultrasound sensor (US) is a crucial component of PAI systems. As PAI technology advances for deeper penetration and higher resolution, the demand for more sensitive and

## 1. Introduction

When an object is exposed to a beam of periodically modulated light, it emits acoustic waves due to the absorption of the illuminating light, resulting in changes in its internal temperature, volume, and structure. This phenomenon, known as the photoacoustic effect, was first discovered by Alexander Graham Bell in 1880.<sup>[1]</sup> Approximately 80 years later, following the emergence

K. Bao, X. Yang  
Zhejiang University  
Hangzhou, Zhejiang 310027, China

K. Bao, C. Sun, L. Li  
Key Laboratory of 3D Micro/nano Fabrication and Characterization of  
Zhejiang Province  
School of Engineering  
Westlake University  
Hangzhou, Zhejiang 310030, China  
E-mail: [lilan@westlake.edu.cn](mailto:lilan@westlake.edu.cn)

K. Bao, X. Yang, C. Sun, G. Rong, M. Sawan, L. Li  
Institute of Advanced Technology  
Westlake Institute for Advanced Study  
Hangzhou, Zhejiang 310024, China  
E-mail: [sawan@westlake.edu.cn](mailto:sawan@westlake.edu.cn)

X. Yang, G. Rong, M. Sawan  
CenBRAIN Neurotech  
School of Engineering  
Westlake University  
Hangzhou 310024, China

C. Tian  
School of Engineering Science  
University of Science and Technology of China  
Hefei, Anhui 230026, China

J. Shi  
Zhejiang Lab  
Hangzhou 311100, China

L. Li  
Westlake Institute for Optoelectronics  
Fuyang, Hangzhou 311421, China

 The ORCID identification number(s) for the author(s) of this article can be found under <https://doi.org/10.1002/lpor.202400414>

DOI: 10.1002/lpor.202400414

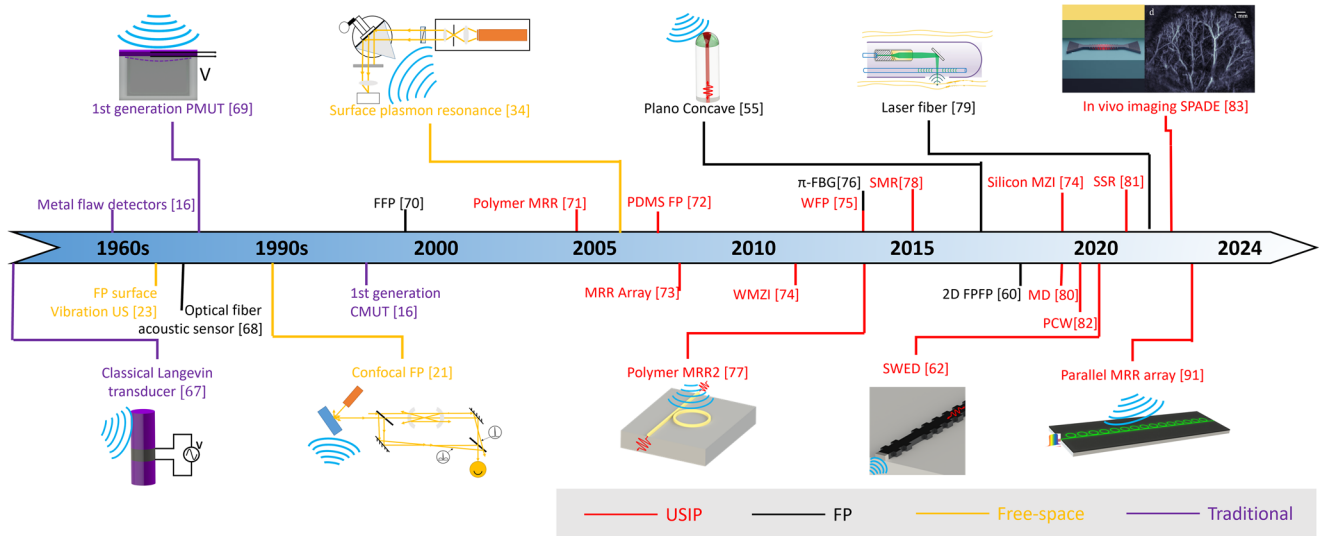


**Figure 1.** Timeline for ultrasound sensors. Classical Langevin Transducer<sup>[67]</sup>; Metal flaw detectors<sup>[16]</sup>; FP surface Vibration US: Fabry-Perot surface vibration ultrasound sensor<sup>[23]</sup>; Optical fiber acoustic sensor<sup>[68]</sup>; 1st generation PMUT: The first generation piezoelectric micromachined ultrasound transducer<sup>[69]</sup>; Confocal FP: Confocal Fabry Perot (ultrasound sensor)<sup>[21]</sup>; 1st generation CMUT: The first generation capacitive micromachined ultrasound transducers<sup>[16]</sup>; FFP: Fiber Fabry-Perot (ultrasound sensor)<sup>[70]</sup>; Polymer MRR: Polymer Micro Ring Resonator (ultrasound sensor)<sup>[71]</sup>; Surface plasmon resonance (ultrasound sensor)<sup>[34]</sup>; PDMS FP: Polydimethylsiloxane Fabry-Perot (ultrasound sensor)<sup>[72]</sup>; MRR Array: Micro Ring Resonator (ultrasound sensor) array<sup>[73]</sup>; WMZI: waveguide Mach-Zehnder interferometer (ultrasound sensor)<sup>[74]</sup>; WFP: waveguide Fabry-Perot (ultrasound sensor)<sup>[75]</sup>;  $\pi$ -FBG:  $\pi$ -phase-shift fiber Bragg Grating (ultrasound sensor)<sup>[76]</sup>; Polymer MRR2: Polymer Micro Ring Resonator 2 (ultrasound sensor)<sup>[77]</sup>; SMR: silicon membrane microring resonator (ultrasound sensor)<sup>[78]</sup>; Plano Concave (ultrasound sensor)<sup>[55]</sup>; 2D FFP: 2D Fabry-Perot fiber probe (ultrasound sensor)<sup>[60]</sup>; Laser fiber<sup>[79]</sup>; MD: Microdisk (ultrasound sensor)<sup>[80]</sup>; Silicon MZI: Silicon Mach-Zehnder interferometer (ultrasound sensor)<sup>[74]</sup>; SWED: silicon waveguide-etalon detector<sup>[62]</sup>; SSR: Split-rib (microring) resonator<sup>[81]</sup>; PCW: polymer coating waveguide (ultrasound sensor)<sup>[82]</sup>; in vivo imaging SPADE: in vivo imaging silicon-photonics acoustic detector<sup>[83]</sup>; Parallel MRR array (ultrasound sensor).<sup>[91]</sup> Reproduced with permission from refs. [34, 55, 62, 67, 69, 79, 83, 91].

scalable broadband ultrasound sensors is increasing. There are numerous applications for USs beyond biomedical imaging. For instance, ultrasound sensing can be applied in various automotive and consumer electronics, such as fingerprint sensing, Advanced Driver Assistance Systems (ADAS), PAI,<sup>[13,14]</sup> and gesture recognition for consumer electronics.<sup>[15]</sup> As a result, the ultrasound sensing market has grown significantly in recent years, with an estimated value of billions of dollars by 2025, according to a report by Yole Développement.<sup>[16]</sup> Given the increasing demand for more sensitive and scalable broadband ultrasound sensors, the technology will continue to evolve and expand into new markets and applications. Various commercial ultrasound sensors utilizing electrical methods to detect ultrasonic signals are readily available, such as Bulk Piezoelectric Ultrasonic Transducers (BPUT), Capacitive Micromachined Ultrasonic Transducers (CMUT),<sup>[17]</sup> and Piezoelectric Micromachined Ultrasonic Transducers (PMUT). However, the miniaturization of these electronics-based sensors is significantly limited, affecting their overall performance. Additionally, the detection bandwidth of these sensors cannot match that of optical sensors, thus limiting their application scenarios.<sup>[18,19]</sup> There is an increasing need for a new generation of photoacoustic/ultrasound imaging in biomedical research and clinical applications, leading to a continuous exploration of new ultrasound sensing technologies, as shown in **Figure 1**. Optical sensors, known for their immunity to electromagnetic interference and ability to offer a range of benefits, including wide detection bandwidth, compact size, large receiving angle, strong responsivity, and, notably,

high sensitivity,<sup>[20]</sup> are expected to play an essential role in the future. Researchers have made attempts to develop free-space optical sensing since the 1970s, including confocal Fabry-Perot interferometer,<sup>[21–23]</sup> Fabry-Perot optical thin film,<sup>[24–27]</sup> Michelson interferometer,<sup>[28]</sup> total internal reflection (TIR),<sup>[29]</sup> metamaterial,<sup>[30]</sup> surface plasmon excitation,<sup>[31–34]</sup> and photonic crystal slabs,<sup>[35,36]</sup> to demonstrate the feasibility of optical sensor structures. Commercial optical ultrasound transducers are emerging.<sup>[25]</sup> However, these free-space optical ultrasound sensors raise special requirements on the structure for roughness, light absorption, shape, etc.<sup>[37]</sup> Ultrasound sensing based on integrated photonics (USIP) and optical fiber sensing<sup>[38–59]</sup> are two promising methods. Although fiber-based ultrasonic sensors<sup>[60]</sup> may also provide high resolution, relatively small size, high sensitivity, and mechanical flexibility,<sup>[61]</sup> the bandwidth is usually limited to 50 MHz and faces scalability challenges. It appears that USIP has superior advantages in terms of miniaturization, sensitivity, and the ability to integrate with electronics for 2D array and functional integration. Moreover, USIP can reach high frequency and wide bandwidth of over 50 MHz or even hundreds of MHz.<sup>[62]</sup> In addition, USIP's compatibility with various material systems presents a significant advantage over fiber sensors, further broadening its potential applications. The integration of the transmitter and receiver onto a single surface has been shown over the USIP platform to greatly simplify the system design of PAI, leading to more compact and efficient systems.<sup>[63,64]</sup> This integrated platform is particularly important for applications such as photoacoustic endoscopy.<sup>[65,66]</sup> Therefore, USIP

could be a promising new technology for ultrasound sensing in the future.

## 2. Performance Metrics of Ultrasound Sensors

There are two main categories of PAI systems: photoacoustic microscopy (PAM) and photoacoustic computed tomography (PACT). In the context of PAM, individual PA signals predominantly emanate from the spatial confinement within the volume defined by the smaller of either the optical focus or the acoustic focus, which further classifies PAM into optical-resolution (OR-) PAM and acoustic-resolution (AR-) PAM. These signals are converted into a 1D image, which portrays the distribution of optical energy deposition along the acoustic axis. This conversion is accomplished by extracting the signal's envelope, which corresponds to the amplitude modulation curve of the radio-frequency PA signal. Conversely, a US matrix in PACT includes three matrix geometries: linear (planar), cylindrical, and spherical. Each ultrasonic transducer element intercepts PA signals over a substantially wide acceptance angle. The collective data gathered from all the transducer elements are employed to reconstruct an image using image reconstruction algorithms for deep imaging. Notably, akin to the triangulation principles employed in the Global Positioning System, this reconstruction process effectively elucidates the spatial distribution of the photoacoustic sources.<sup>[10]</sup> Therefore, resolution is the primary focus in PAMs, while PACTs care more about the imaging depth. The resolution and imaging depth rely on the performance of USs and other factors affecting the imaging quality.

### 2.1. Resolution - CENTRAL Frequency and Bandwidth

In PAM, the theoretical resolution of the systems is given by<sup>[84]</sup>

$$R_{PAM, A} = \frac{0.88v_s}{B} \quad (1)$$

$$R_{AR-PAM, L} = \frac{0.71v_s}{NA_a \cdot f} \quad (2)$$

$$R_{OR-PAM, L} = \frac{0.51\lambda}{NA_o} \quad (3)$$

where A denotes axial resolution, and L denotes lateral resolution;  $v_s$  is the velocity of sound in the medium, and  $B$  is the bandwidth of the ultrasound sensor;  $NA_a$  and  $NA_o$  are the numerical aperture of the lens used to focus sound waves and the numerical aperture of the lens used to focus the illumination light, respectively;  $\lambda$  is the wavelength of the illumination light.

From Equation (1), the axial resolution of PAM has a significant relationship with the frequency of photoacoustic signals. The generated photoacoustic signal is a broadband ultrasound signal with bandwidth from hundreds of kHz to several GHz,<sup>[105]</sup> while the ultrasound receiver is a band-pass filter over the frequency spectrum, as shown in Figure 2a. We define the central frequency  $f_C$  of the ultrasound sensor as the average of low-cutoff frequency,  $f_L$  and high-cutoff frequency,  $f_H$ , (to note that

in many articles the central frequency refers to the highest response acoustic frequency) and bandwidth,  $B$ , to be  $f_H - f_L$ . Typically,  $-6$  dB bandwidth is used to characterize the performance of USs. In many scenarios, fraction bandwidth (FB), defined by  $B/f_C \times 100\%$ , is more convenient to describe the performance of USs. Therefore, considering USs, the axial resolution of PAM systems and lateral resolution of AR-PAM are limited to be:

$$R_{PAM, A} = \frac{0.88v_s}{B} = \frac{0.88v_s}{f_C \times FB} \quad (4)$$

$$R_{AR-PAM, L} = \frac{0.71v_s}{NA_a \cdot f_H} = \frac{0.71v_s}{NA_a \cdot (f_C + B/2)} = \frac{0.71v_s}{NA_a \cdot f_C (1 + FB/2)} \quad (5)$$

In PACT, the theoretical resolution of the systems is given by<sup>[106]</sup>

$$R_{PACT, A} = 0.6 \lambda_H = \frac{0.6v_s}{f_H} = \frac{0.6v_s}{f_C + B/2} = \frac{0.6v_s}{f_C (1 + FB/2)} \quad (6)$$

$$R_{PACT, Llp} = \sqrt{R_{PACT, A}^2 + (2a)^2} \quad (7)$$

$$R_{PACT, Lcs} = \sqrt{R_{PACT, A}^2 + [(d/r)(2a)]^2} \quad (8)$$

where  $Llp$  and  $Lcs$  denotes the lateral resolution of linear and planar sensor matrices and cylindrical and spherical sensor matrices, respectively;  $2a$  denotes the aperture or size of sensor elements;  $d$  is the distance from the imaging points to the scanning center;  $r$  is the radius of the cylindrical and spherical sensor matrix.

PA signals are broadband signals. Each frequency carries information. Thus, a full (200%) bandwidth is desired to enhance the reconstruction of the image. In the experiment, resolutions are determined by the point spread function (PSF).<sup>[107]</sup> PSF can be expressed as:<sup>[108]</sup>

$$PSF(d) = \frac{k_C^2}{2\pi^2 d} \left\{ (1 + 0.5FB)^2 J_1 \left[ (1 + 0.5FB) k_c d \right] - (1 - 0.5FB)^2 J_1 \left[ (1 - 0.5FB) k_c d \right] \right\} \quad (9)$$

where  $d$  is the distance to the center;  $k_C = 2\pi f_C/v_s$ ;  $J_1$  is the first-order spherical Bessel function of the first kind.

As shown in Figure 2c, PSF's full width at half maxima (FWHM) is the experimental resolution for PAI systems. A larger  $FB$  will result in a less oscillating PSF, leading to a finer spatial resolution and a clearer image, as shown in Figure 2c. In Figure 2b, traditional USs can hardly get a  $FB > 100\%$  while optical USs tend to have  $FB > 100\%$ , and most USIP devices even have a full  $FB$ . Therefore, PAI systems employing USIP will get finer spatial resolution. In Figure 2d, as the central frequency drops, the FWHM of the PSF curve broadens, and the curves become more oscillating, in agreement with Equations (4) and (5).

From Equations (4) to (8), a high cut-off frequency is required to achieve a high axial resolution. Figure 2b shows that optical ultrasound detection, especially USIP, shows great superiority

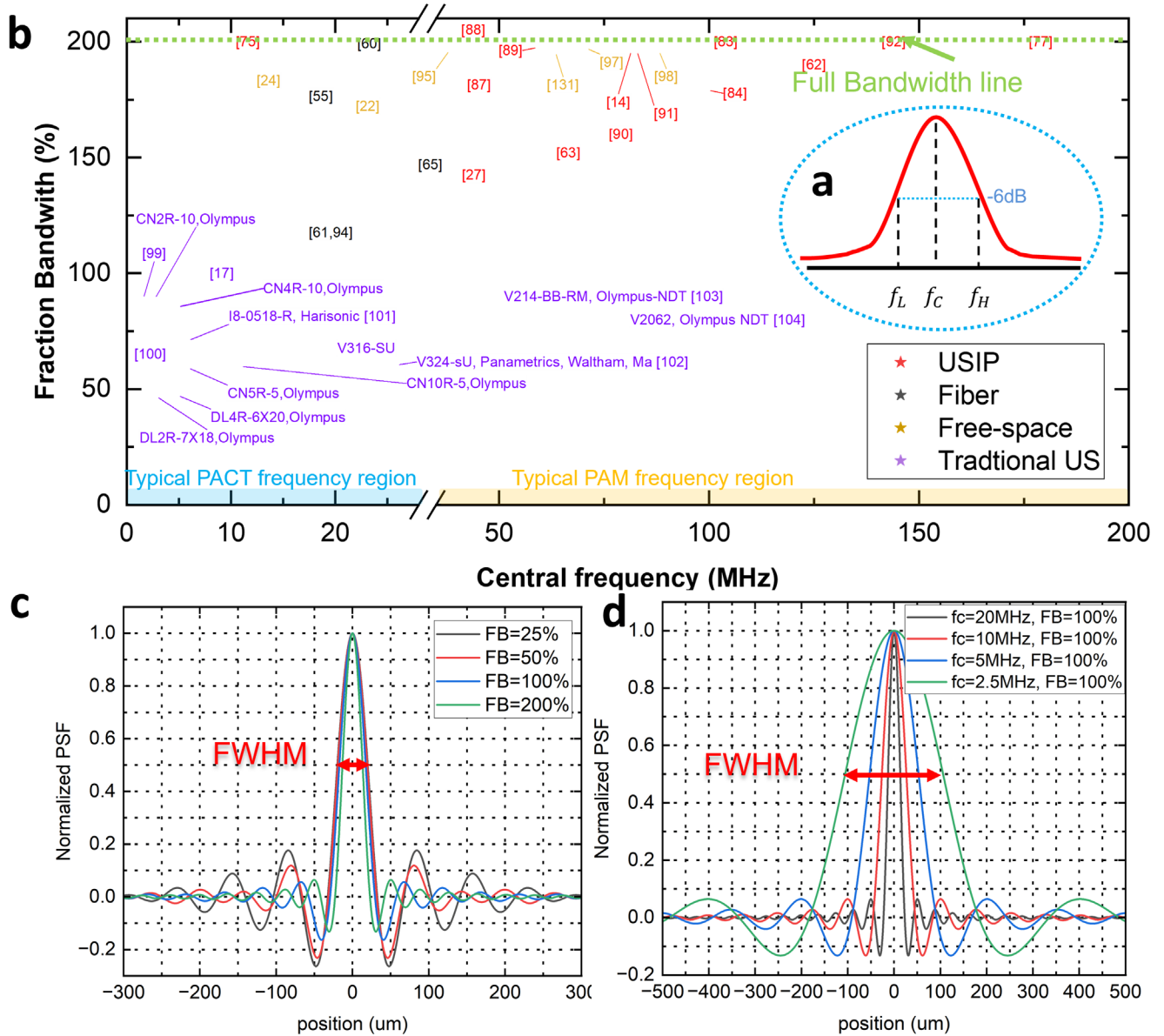


**Figure 2.** Ultrasound central frequency and bandwidth. a) Definition of  $f_L, f_C, f_H$  and  $B$ ; b) central frequency and bandwidth (@-6 dB) reported. c) Simulated normalized PSFs of USs under different FB ( $f_C = 20$  MHz); d) Simulated normalized PSFs of USs under different  $f_C$  ( $FB = 100\%$  @-6 dB). Reference in (b): [14, 17, 22, 24, 55, 60–62, 65, 72, 75–77, 83, 85–104].

among the high-frequency ultrasound sensing methods. In addition, many USIP devices have more flat acoustic responses over high-frequency regions with a  $FB > 100\%$  while traditional USs tend to have a  $FB < 100\%$ , which results in a higher likelihood of information loss in ultrasound signals. And USIP devices can cover both PAM and PACT acoustic frequency regions, leading to broader applications.

An optical ultrasound sensing element's bandwidth is mainly determined by the ultrasound wave propagation within the cavity and the optical resonance.<sup>[109]</sup> The geometry-limited cut-off frequency,  $f_{H-P}$ , is determined as:<sup>[109]</sup>

$$f_{H-P} = \frac{v_s}{2h} \quad (10)$$

where  $h$  is the thickness of the sensor element. And the resonance-limited cut-off frequency,  $f_{H-R}$ , has an inverse proportion to the time constant,  $\tau$ , of the resonance:<sup>[109]</sup>

$$f_{H-R} = \frac{1}{\tau} = \frac{\omega}{Q} \quad (11)$$

where  $\omega$  is the angular frequency of the propagating light wave, and  $Q$  is the quality factor of the resonant cavity. For example, a  $Q \sim 10^6$  for 1550 nm wavelength light results in a  $f_{H-R} \sim 12$  GHz. A typical thickness of USIP devices ( $2 \mu\text{m}$ ) results in (assuming  $v_s = 1500 \text{ m/s}$ ) a  $f_{H-P} \sim 400$  MHz. Therefore,  $f_{H-P}$  often domains in USIP devices.

The resolution of ultrasound imaging is significantly influenced by the relationship between the cut-off frequency of the

ultrasound detector and the pressure relaxation time of the target. Specifically, when considering a spherical target, the thermal confinement threshold time  $\tau_{th}$  and the stress confinement threshold time  $\tau_{st}$  are respectively:<sup>[106]</sup>

$$\tau_{th} = \frac{D^2}{4D_T} \quad (12)$$

$$\tau_{st} = \frac{v_s}{D} \quad (13)$$

where  $D_T$  is the thermal diffusivity ( $\approx 0.14 \text{ mm}^2/\text{s}$  for soft tissue<sup>[106]</sup>),  $D$  is the diameter of the target, and  $v_s$  is the speed of sound in the medium. To obtain high-quality imaging, researchers should select an ultrasound detector that cover the frequency range of generated photoacoustic signals. Optimal photoacoustic imaging is achieved when the cut-off frequencies of the generated photoacoustic signals fall within the ultrasound detector's response region. Then the ideal high cut-off frequency should be  $f_H > 1/\tau_{st}$  (for  $\tau_{th} \ll \tau_{st}$ ). From this, we can derive that the suitable thickness for ultrasound detectors, when resonance limitations are negligible, is approximately  $h < 0.5D$ .

## 2.2. Imaging Depth - Sensitivity and NEP

Imaging depth is a critical advantage of PAI compared to optical imaging due to the deep penetration of acoustic waves. Indeed, maximum imaging depth is mainly decided by the acoustic attenuation and the minimum detectable acoustic signal. Acoustic attenuation is due to scattering, absorption, diffusion, and reflection. In PAI, absorption attenuation is the main concern. Absorption attenuation is frequency-dependent and can be written as:<sup>[110]</sup>

$$\alpha_{ab} = \beta f^n \text{ (dB/cm)} \quad (14)$$

where  $\beta$  is the frequency-dependent absorption attenuation coefficient of the medium;  $f$  is the acoustic frequency and  $n$  is the exponent determined by the medium (in water  $n = 2$ ). The frequency-dependent absorption attenuation coefficient in water is about  $0.00139 \text{ dB/(cm} \times \text{MHz}^2)$ .<sup>[111]</sup> And the reflection loss can also be quantified:<sup>[14]</sup>

$$\alpha_r = \left( \frac{Z_{in} - Z_{out}}{Z_{in} + Z_{out}} \right)^2 \quad (15)$$

where  $Z_{in}$  and  $Z_{out}$  are the acoustic impedances of the input and output materials, respectively. The acoustic impedance of water is  $1.5 \text{ MRayl}$ . The air-coupled ultrasound detection will induce an extra interface, resulting in a high  $\alpha_r$ . For air-coupled USs,  $\alpha_r$  is ultra-high,  $\approx 122 \text{ dB/cm}$  for  $10 \text{ MHz}$  ultrasound,<sup>[112]</sup> while in water, the  $\alpha_r$  is only  $0.139 \text{ dB cm}^{-1}$  for  $10 \text{ MHz}$  ultrasound. Therefore, the air-coupled USs raises higher requirements for the sensitivity of ultrasound detectors.<sup>[37]</sup> PAMs typically have a limited imaging depth of a few millimeters due to the absorption and reflection loss of acoustic waves in tissues at high frequencies. However, PACT can achieve an imaging depth of  $\approx 10 \text{ cm}$  by utilizing low-frequency ultrasound signals.<sup>[10]</sup>

In fact, the maximum imaging depth is determined by the optical absorption in an illuminated medium and the minimum detectable acoustic pressure of USs, which is defined as noise-equivalent pressure (NEP), in units of Pa.<sup>[113]</sup> NEP is frequency-dependent since the noise level increases as the frequency increases.<sup>[77]</sup> An ideal US should maintain a low and flat NEP over a large acoustic bandwidth. So, the NEP spectral density (NEPD), in the unit of  $\text{Pa}/\sqrt{\text{Hz}}$ , is also applied in characterizing USs, which means a NEP over a bandwidth. Note that NEPD is also called NEP in some literature. In traditional electrical USs, the noise consists of thermal noise, sensor resistance noise, and preamplifier-induced noise. The NEP can be expressed as:<sup>[105]</sup>

$$NEP_{\text{traditional}}(f) = \sqrt{k_B T \left[ 1 + \frac{F_n}{\eta(f)} \right] \frac{Z_a}{A}} \quad (16)$$

where  $k_B$  is the Boltzmann constant, and  $T$  is the temperature;  $A$  is the sensing area,  $\eta(f)$  is the detector efficiency;  $F_n$  is the noise factor of preamplifier noise (low-noise preamplifier  $F_n \approx 2$ );  $Z_a$  is the acoustic impedance. Meanwhile, in optical detection, the level of noise depends on the specific used detection method. Intensity detection is the most widely used detection method in USIP. With intensity detection, the noise is caused by laser power fluctuation  $N_{RIN}$ , laser statistic spectral instability  $N_{spec}$ , shot noise  $N_{shot}$  and Johnson noise coming from photodetector (PD) transforming optical signal into electrical signal, and environmental temperature fluctuation  $N_{therm}$ .<sup>[114,115]</sup>

$$NEP_{USIP-id} = \sqrt{N_{RIN}^2 + N_{spec}^2 + N_{shot}^2 + N_{Johnson}^2 + N_{therm}^2} \quad (17)$$

$$N_{RIN} = S_{RIN} BR_{es} P_L G (T/S + P) \quad (18)$$

$$N_{spec} = R_{es} P_L G B_{laser} \lambda^2 / c \left( \frac{dT}{d\lambda} + SP \frac{dP}{dT} \frac{dn_{eff}}{dP} \frac{d\lambda}{dn_{eff}} \frac{d^2 T}{d\lambda^2} \right) / S \quad (19)$$

$$N_{shot} = \sqrt{2eB/SR_{es}P_L(T/S+P)G_M^x G} \quad (20)$$

$$N_{Johnson} = \sqrt{4k_B T_i B G / S} \quad (21)$$

$$N_{therm} = \frac{dP}{d\lambda} \frac{d\lambda}{dn_{eff}} C_T \Delta T_i / (G G_M R_{es}) \quad (22)$$

where  $S_{RIN}$  is the power spectral density;  $R_{es}$  is the responsivity of the PD;  $P_L$  is the laser power;  $G$  is the transimpedance gain;  $S = \frac{dV}{dP}$  is the output sensitivity;  $V$  is the output electrical signal;  $T$  is the normalized transmission;  $P$  is the acoustic pressure;  $B_{laser}$  is the laser linewidth;  $c$  is the velocity of light;  $n_{eff}$  is the effective index of the waveguide;  $e$  is the charge of electrons;  $G_M$  is the gain of the PD and  $1 \leq x \leq 2$  is the excess noise index;  $C_T$  is the thermo-optic coefficient of the waveguide;  $\Delta T_i$  is the surround temperature change. Thus, there will be a trade-off between

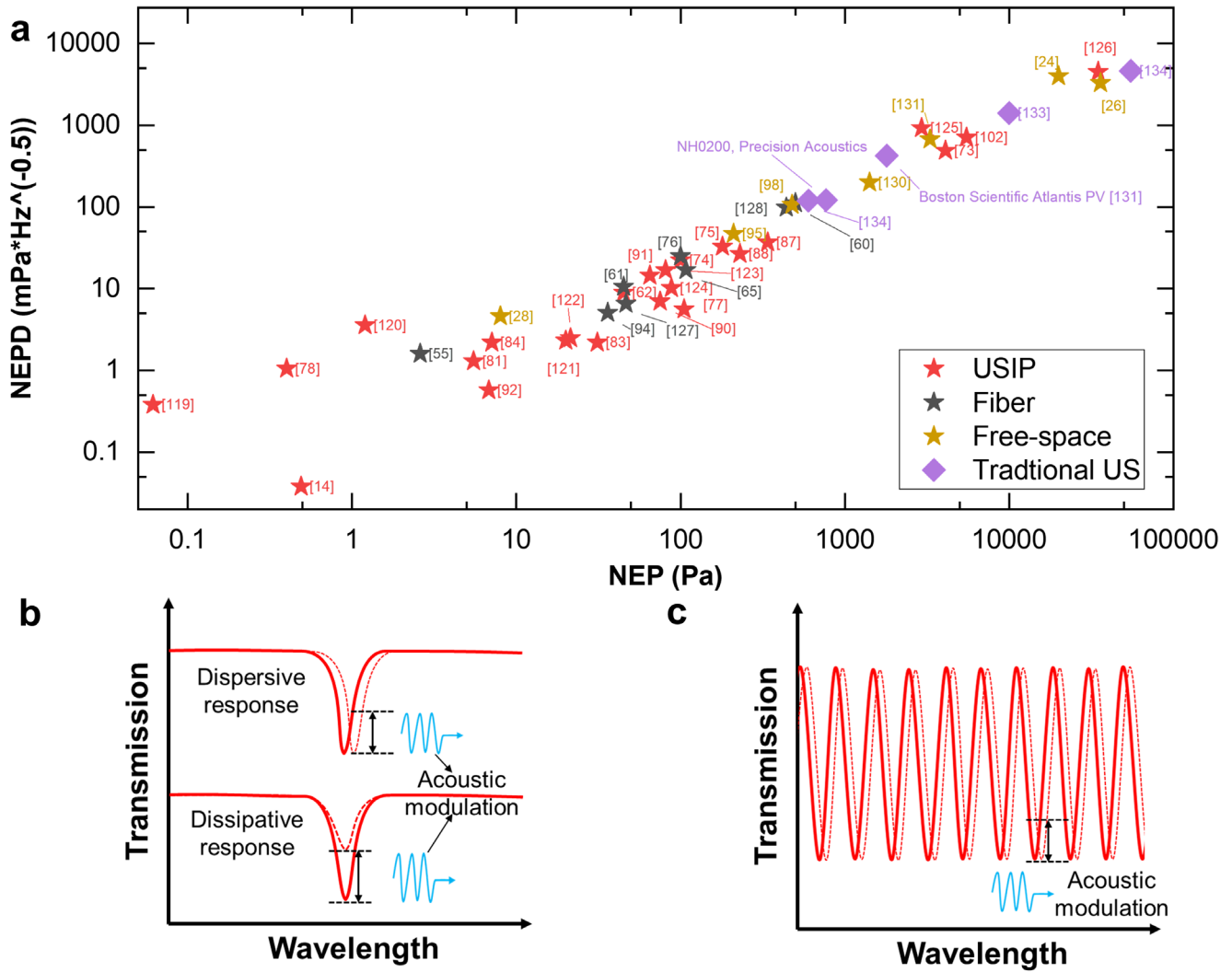


**Figure 3.** Sensitivity of USs. a) Comparison of USs' NEP. b) Principles of acoustic modulation induced by dispersion and dissipation.<sup>[119]</sup> c) Principle of acoustic modulation induced by interference phase change. (Reference in (a): [14, 24, 26, 55, 60–62, 65, 73–78, 81, 83, 86, 87, 89–92, 94, 95, 98, 102, 120–135]).

B and NEP, according to Equations (17)–(22). While there is an acoustic resonant structure like a membrane structure, things will be different. The noise consists of thermal-mechanical noise  $S_{thermal}$ , and probe-laser-induced shot noise  $S_{shot}$ .<sup>[116]</sup> The NEP can be expressed as:<sup>[80,116,117]</sup>

$$NEP_{membrane} = \frac{1}{r\zeta A} \sqrt{S_{thermal} + \frac{S_{shot}}{|\chi|^2}}$$

$$= \frac{1}{r\zeta A} \sqrt{2m\gamma k_B T_t + \frac{\kappa(1 + 4\omega_a^2/\kappa^2)}{16\eta NG^2 |\chi|^2}} \quad (23)$$

$$N = \frac{QP_L}{\hbar\omega^2} \quad (24)$$

where  $r$  is the pressure participation ratio;  $\zeta$  is the spatial overlap of the acoustic incident area and the total sensing area;  $m$  is

the effective mass of the sensor;  $\omega_a$  is the angular frequency of the acoustic waves;  $\gamma$  is the intrinsic mechanical damping rate;  $\kappa$  is optical energy decay rate;  $\chi$  is a mechanical susceptibility function;  $N$  is the number of photons in the cavity;  $\hbar$  is the Dirac constant.

USIP devices have a low NEP and NEPD, as shown in **Figure 3a**. Most USIP devices appear to have a NEP lower than  $10^3$  Pa. Though a focusing laser can generate photoacoustic signals  $>50$  MPa,<sup>[118]</sup> the photoacoustic signals are typically below  $10^3$  Pa over hundreds of MHz in PAI,<sup>[106]</sup> resulting in a NEPD of hundreds of  $mPa/\sqrt{Hz}$ . Most traditional electrical USs used in PAI have a high NEPD over hundreds of  $mPa/\sqrt{Hz}$ <sup>[76]</sup> and, therefore, are not ideally suitable for PACT implementation, while high-end USIP devices typically have a low NEPD at several  $mPa/\sqrt{Hz}$ .<sup>[62,81]</sup> Compared to fiber-based USs, USIP also demonstrates significantly lower NEP. A low NEP indicates a high signal-to-noise ratio (SNR), which translates to a high

**Table 1.** Stress-optical coefficient and Young's modulus of some commonly used materials in integrated photonics. The refractive index is either obtained from the website refractiveindex.info (O) or measured by ellipsometer (M) (RC2 XI+, J.A. Woollam).

Material	Stress-optical coefficient [GPa <sup>-1</sup> ]	Refractive index @ 1550nm	Young's modulus [GPa]	Acoustic Impedance (Rayl)	References
Si	$C_1 = -11.35 \times 10^{-3}$ $C_2 = 3.65 \times 10^{-3}$	3.673 (O)	130–188	$1.95 \times 10^7$	[82, 136, 137]
Si <sub>3</sub> N <sub>4</sub>	$3.4(\pm 0.1) \times 10^{-3}$	2.030 (M)	300–330	$3.5 \times 10^7$	[138–140]
SiO <sub>2</sub>	$C_1 = 1.17 \times 10^{-3}$ $C_2 = 3.73 \times 10^{-3}$	1.444 (O)	12–89	$1.36 \times 10^7$	[82, 141]
TiO <sub>2</sub>	$-(1.79–2.14) \times 10^{-2}$	2.32(@ 1310 nm) (M)	72(±0.3)	$1.7 \times 10^7$	[142, 143]
SU8	$-2.6 \times 10^{-1}$	1.575 (M)	2.0	$3.3 \times 10^6$	[144–146]
GSS (Ge <sub>23</sub> Sb <sub>7</sub> S <sub>70</sub> )	$C_R = (1.32 \pm 0.08) \times 10^{-1}$ $C_\theta = (3.42 \pm 0.08) \times 10^{-1}$	2.220 (O)	16.4	/	[144]
GSSe (Ge <sub>28</sub> Sb <sub>12</sub> Se <sub>60</sub> )	/	2.680 (M)	22.1	/	[147]
Polydimethylsiloxane (PDMS)	>1	1.404 (O)	$1.4 \times 10^{-3}$	$1.48 \times 10^6$	[14, 83, 148]
Polystyrene (PS)	$C_1 = 4.8 \pm 0.3 \times 10^{-2}$ $C_2 = 2.9 \pm 0.3 \times 10^{-2}$ @632.8nm	1.565 (O)	0.3±0.1	$2.47 \times 10^6$	[85, 149]
Polymethyl methacrylate (PMMA)	$-1.085 \times 10^{-1}$	1.472 (O)	3.24	$3.25 \times 10^6$	[149–151]

1Rayl = 1 kg · m<sup>-2</sup>s<sup>-1</sup>.

intrinsic sensitivity. It is important to note that the sensitivity of optical ultrasound cannot be directly compared to electrical ultrasound due to different measurement methods. Instead, we compare them using NEP. In traditional ultrasound systems, sensitivity is defined as the ratio of output voltage to acoustic pressure. In optical ultrasound systems, sensitivity is defined as the ratio of optical transmission change to acoustic pressure. Based on commonly used structural designs, the sensitivity analysis of USIP is conducted accordingly.

Based on detection principles, USIP can be categorized into resonant and non-resonant methods. In resonant methods, a complete description of acoustic-optic interaction includes dispersion and dissipation.<sup>[80,119]</sup> As shown in Figure 3b, dispersion induces a change in resonant cavity length to shift the resonant wavelength, and dissipation induces intrinsic optical loss or cavity decay rate change. Researchers often use resonant cavities for high-frequency acoustic detection where dissipation is negligible and hard to measure due to high Q factors. Therefore, the resonant wavelength shift is often used to characterize ultrasound signals. The detection process involves introducing light of a specific wavelength into the resonant cavity, targeting the point on the transmission curve with the sharpest slope. It is believed that the power of the modulated output light exhibits a linear correlation with the ultrasound signal. Therefore, resonant USIP devices' normalized sensitivity can be written as:<sup>[92]</sup>

$$S_{resonant} = \frac{dT}{dP} = \frac{dT}{d\lambda} \frac{d\lambda}{dn_{eff}} \frac{dn_{eff}}{dP} \quad (25)$$

where  $T$  is the transmission and  $P$  is the acoustic pressure;  $n_{eff}$  is the effective refractive index of the resonant cavity. In a resonant cavity, there is an equation:

$$n_{eff}l = m\lambda_r \quad (26)$$

where  $l$  is the resonant cavity length and  $\lambda_r$  is the resonant wavelength. Considering a small perturbation in  $n_{eff}$  and  $\approx \lambda_r$ :

$$\frac{d\lambda}{dn_{eff}} \approx \frac{d\lambda_r}{dn_{eff}} = \frac{l}{m} = \frac{\lambda_r}{n_{eff}} \approx \frac{\lambda}{n_{eff}} \quad (27)$$

And  $\frac{dT}{d\lambda}$  is linearly proportional to the cavity Q and  $\frac{dn_{eff}}{dP}$  is the stress-optical coefficient of the material,  $C$ . Then Equation (25) can be expressed as:

$$S_{resonant} = A Q \frac{\lambda}{n_{eff}} C \quad (28)$$

where  $A$  is a constant.

From Table 1, we can approximately get an empirical equation:

$$E \approx \frac{n}{C} \quad (29)$$

where  $E$  is Young's modulus,  $n$  is the refractive index. Since  $C$  of materials is challenging to measure, we can refer to  $E$ . Then Equation (28) can be written as:

$$S_{resonant} \approx A Q \lambda / E \quad (30)$$

From Equation (30), when we design a USIP device, we can choose low Young's modulus materials with a high Q factor and ensure it operates at longer wavelengths.

For non-resonant USIPs, the Mach-Zehnder interferometer is the conventional structure. There are two arms, one for sensing and the other for reference. The detection principle is shown in Figure 3c. The sensitivity can be expressed as:<sup>[120]</sup>

$$S_{non-resonant} = \alpha I_{input} \left| \frac{dT}{dP} \right| \quad (31)$$

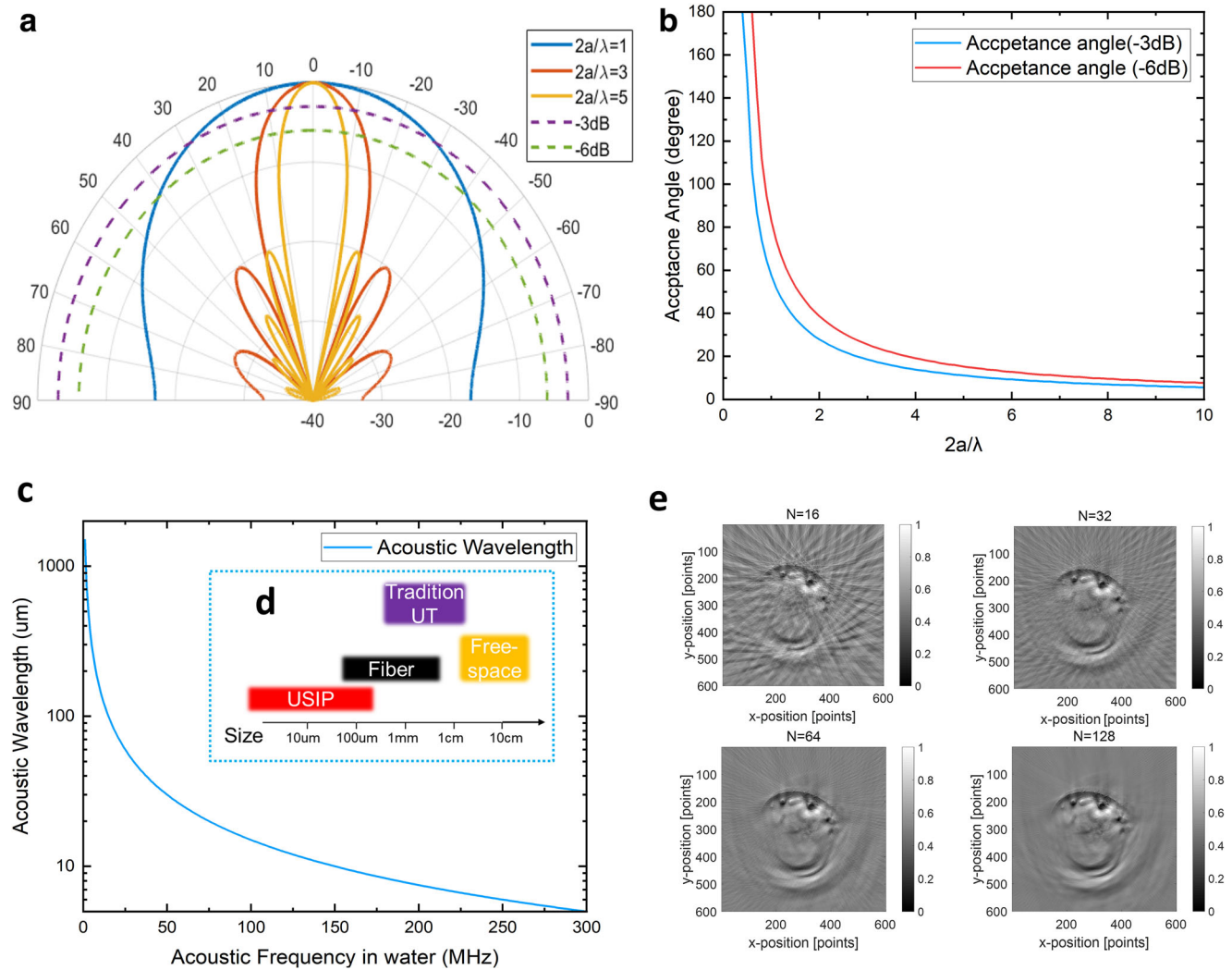


**Figure 4.** Illustrations of some other factors affecting PA image quality. a) Directional acoustic response over different  $2a/\lambda$  ( $r$  axis: dB;  $\theta$  axis: degree); b) simulated acceptance angle under different  $2a/\lambda$ ; c) acoustic wavelength in water under different frequencies ( $\nu_s = 1500 \text{ m s}^{-1}$ ); d) typical size of USs; e) reconstructed images under different numbers (N) of sensor elements ( $f_c = 5 \text{ MHz}$ , aperture:  $1.32 \text{ mm} \times 20 \text{ mm}$ ) from a customized half-ring ( $r = 55 \text{ mm}$ ) 128-channel PACT system (TsingPai Technology Co., Ltd.). We use  $N = 16, 32, 64,$  and  $128$  channels to reconstruct a PA image of a finger, respectively. The channels on each image are chosen with no overlap and are uniform on the half ring.

where  $\alpha$  is the overall loss and  $I_{input}$  is the input light power. Therefore, according to Equations (25)–(31), a soft and low-loss material is ideal for non-resonant USIPs. And the broad bandwidth of ultrasonic systems can be achieved through their high sensitivity across a wide range of frequencies.

According to Equations (30) and (31), USIP devices could achieve high Q factors and have more material alternatives, resulting in a high detection sensitivity among optical USs.

### 2.3. Image Quality –Size and Element Number

Other factors, aside from resolution and imaging depth, such as the size and element number of the detectors, will also affect the PA image quality. In addition to the factors discussed, various other effects also play a significant role in determining image quality in practical applications of USIP. These in-

clude surface acoustic waves,<sup>[83]</sup> reverberations,<sup>[83,89]</sup> mechanical resonances,<sup>[80,112]</sup> diffraction from edges,<sup>[83]</sup> and non-linear effects in optical resonators,<sup>[89,152]</sup> among others.

The US's size or aperture is a parameter that significantly influences the image quality. In Equations (7) and (8), we know that the size of the US will influence the lateral resolution of PACT systems. Meanwhile, large size will also influence the image quality due to its directional acoustic response because the photoacoustic signals are not parallel in space. The directional response difference  $D(\theta)$  can be expressed as:<sup>[108]</sup>

$$D(\theta) = \frac{2J_1(ka \sin \theta)}{ka \sin \theta} \quad (32)$$

where  $k$  is the wave vector of the photoacoustic signal.

From Figure 4a,b, it can be observed that a lower value of  $2a/\lambda$  leads to a more omnidirectional response. As shown in Figure 4c,

a large acceptance ( $\sim -6$  dB  $> 40$  degrees) needs a  $2a/\lambda < 1.95$ . And at  $-3$  dB, the ratio should be  $< 1.4$ . As shown in Figure 4c, the size should be further minimized at a high frequency. For example, if we desire a 50 MHz photoacoustic signal, our sensor should have a size  $< 60$   $\mu\text{m}$  for reasonable high-quality imaging. Figure 4d illustrates the dimensions of the USs, with USIP devices demonstrating the smallest sizes, even within the submicron range.<sup>[62]</sup> Furthermore, the sensor's shape significantly impacts image quality by affecting its angular response. For an in-depth analysis, refer to the eighth figure in reference [109].

In PACT systems, a sensor matrix is required for fast detection. We can see from Figure 4e that reconstructed finger image quality differs under detector element numbers of 16, 32, 64, and 128. Alexander Dima et al.<sup>[135]</sup> first studied the sensor element number's influence. A high-quality reconstructed image requires a high-density and large element number sensor matrix. The state-of-the-art traditional-US-based PACT system has a sensor element number of 1024.<sup>[20,153]</sup> Fiber sensors can integrate over 50 000 elements on a single optical fiber.<sup>[60]</sup> However, these sensors have to be used in free-space galvanometer scanning, greatly complicating the detection system. And the integration of a large number of elements in USIP devices remains largely unreported due to technical limitations and challenges. The largest USIP device's element number integrated with a matrix on a single bus waveguide is 15.<sup>[83,91]</sup> Indeed, the integration of USIP sensor matrix is seen as a promising avenue for future research, especially in the field of PACT. Theoretically, with wavelength-division-multiplexing (WDM) technology,<sup>[154–157]</sup> we can integrate hundreds to thousands of elements on a bus waveguide. However, practical applications face certain challenges. For instance, in the case of MRR sensors, accurate control over the resonant wavelength is difficult due to fabrication errors, causing the resonant wavelength to fall almost randomly on the transmission spectrum. Additionally, it is crucial that all resonant wavelengths fall within a single free-spectral range (FSR) to differentiate them over the spectrum. The spectrum requires a certain wavelength range, which is inversely proportional to the Q. Therefore, the practical number of USIP device integration is determined by the Q factor and the FSR. Furthermore, each resonator cavity introduces insertion loss, which becomes significant under a low Q factor. Hence, the element number,  $Num \propto \frac{FSR \times Q}{\lambda}$ , if the insertion loss is negligible. Nevertheless, researchers have proposed some FSR-free cavity designs that may provide a solution to these limitations.<sup>[156,157]</sup>

While the spatial averaging model suggests that sensor size exclusively determines the sensor's spatial response, this is often not the case in practical scenarios.<sup>[158]</sup> Effects such as surface acoustic waves, reverberations, mechanical resonances, diffraction from edges, and optical nonlinear effects can also significantly impact the sensor's ultrasound response. In 2022, Amir Rosenthal's group demonstrated that an optimal acoustic impedance match for the US can mitigate the parasitic effects of acoustic reverberation and surface acoustic waves (SAWs).<sup>[83]</sup> Subsequently, in 2023, they also illustrated that a phase monitoring scheme based on the Mach-Zehnder interferometer can effectively suppress laser phase noise. They further showed that a larger mode volume can reduce the impact of nonlinear effects, thus enabling a high tolerance for interrogation powers.<sup>[89]</sup>

### 3. Optical Device Structure Designs for Ultrasound Sensing

Typically, there are four types of structures for USIP: Microring Resonator (MRR),<sup>[14,78,159–162]</sup> Fabry-Perot (FP) resonator,<sup>[75,163]</sup> Bragg Grating (BG),<sup>[62,164–167]</sup> and Mach-Zehnder interferometer (MZI),<sup>[113,168,169]</sup> as shown in Figure 5a–d. We will introduce each of these designs individually in this section.

#### 3.1. Resonant Method

##### 3.1.1. Microring Resonator Structure

As shown in Figure 5a, an MRR comprises a ring cavity and a straight waveguide, enabling light coupling into and out of the resonator. The structures are subject to deformation induced by ultrasound waves, affecting both the ring waveguide (mainly the cross section) and the coupling region, resulting in a shift in the resonant wavelength, shown in Figure 3b.<sup>[71]</sup> The deformation in the cross-section mainly induces dispersion, and the coupling region mainly induces dissipation. As mentioned before, we often neglect the deformation effect in the coupling region. In the following section, we classified and reviewed MRRs based on various optical materials.

**Polymer MRR:** As shown in Table 1, Polymer materials exhibit high levels of photoelastic performance. According to Equation (30), low Young's modulus makes them a popular choice for researchers developing USIP devices on Polymer MRRs. PS is a popular material due to its high stress-optical coefficient and low Young's modulus, as shown in Table 1. Guo, L. Jay's group has been fabricating a series of PS MRRs using nanoimprint technology at near 1550 nm wavelength since 2002.<sup>[170]</sup> In 2004, they first applied a PS MRR for ultrasound detection.<sup>[71]</sup> The first PS MRR, with a diameter of 60  $\mu\text{m}$ , had a relatively low Q factor of  $\approx 1000$  and a  $-3$  dB bandwidth of only about 10 MHz. The measured sensitivity was  $3 \times 10^{-3}$  RIU/kPa. They later achieved a PS MRR with an intrinsic sensitivity ( $d\lambda/dP$ ) of 21 pm MPa $^{-1}$  and a diameter of 95  $\mu\text{m}$  in 2007.<sup>[85]</sup> The NEP is measured to be 150 kPa over a bandwidth of 40 MHz ( $2.4$  Pa/ $\sqrt{\text{Hz}}$ ). Then in 2008, a  $-3$  dB bandwidth of over 90 MHz and a Q factor of 6000 was achieved.<sup>[87]</sup> They applied their polymer MRR in PAI in 2008,<sup>[161]</sup> achieving an axial resolution of 90  $\mu\text{m}$  and a lateral resolution of 150  $\mu\text{m}$ , and later obtained a high resolution of 12.5  $\mu\text{m}$  in 2009.<sup>[161]</sup> The Q factor was improved to be  $\approx 1.5 \times 10^5$ <sup>[125]</sup> and even  $5.1 \times 10^5$ .<sup>[123]</sup> Moreover, the PAI system was improved to have an axial resolution of 21  $\mu\text{m}$  and a lateral resolution of 55  $\mu\text{m}$ .<sup>[122,171,172]</sup> In 2014, they fabricated an MRR with a  $-3$  dB bandwidth of 350 MHz, working near 780 nm, the most broadband USIP device ever reported.<sup>[77]</sup> A sub-3  $\mu\text{m}$  axial resolution was achieved with this MRR. Hao F. Zhang and his co-workers also significantly contributed to polymer MRR USIP.<sup>[64,92,173,174]</sup> Their group used SU-8 MRRs by e-beam lithography on PAI. Their SU-8 MRR achieved a bandwidth of 140 MHz<sup>[92]</sup> with an NEP of 6.8 Pa and 250 MHz with an NEP of 352 Pa.<sup>[64]</sup> However, to maintain a high Q factor the sensors have work at wavelength near 780 nm. According to Equation (30), the sensitivity can still be improved. Later, they used nanoimprinted PS MRR with a

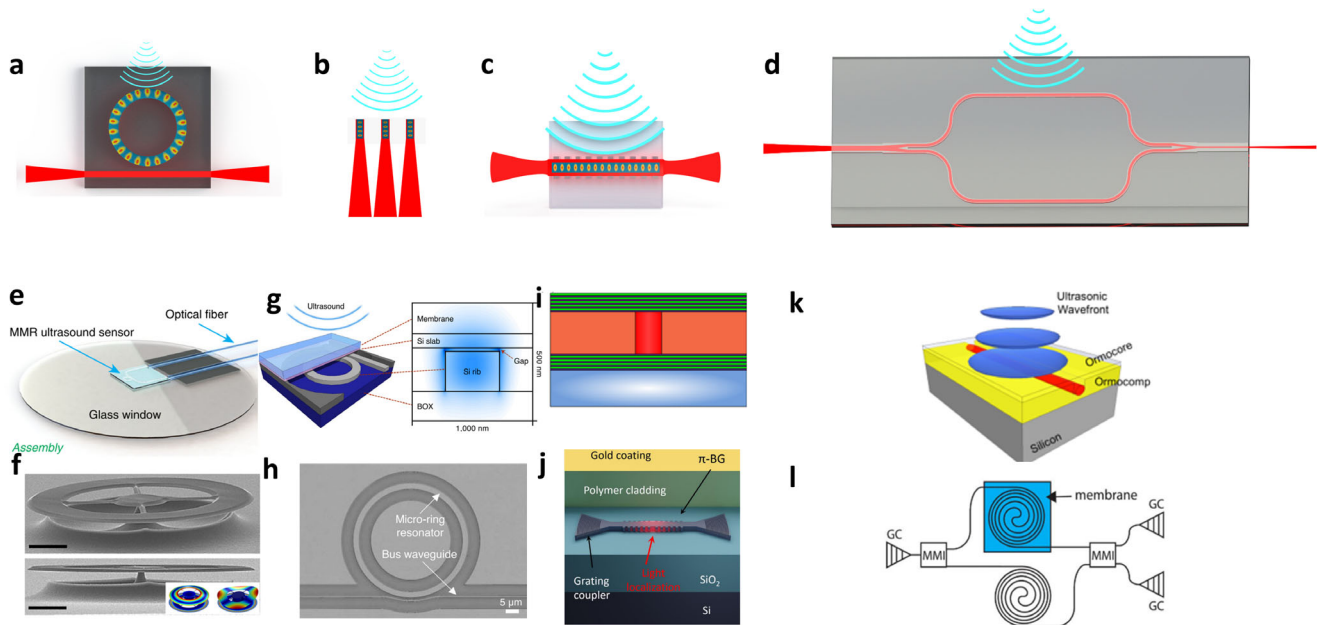


**Figure 5.** Schematics of reported USIP. a–d) Schematics of USIP devices on MRR, FP, BG, and MZI, respectively. e) MRR fabricated by soft nanoimprinting lithography for PAMI<sup>[14]</sup>; f) suspended microdisk US (scale bar: 20  $\mu\text{m}$ )<sup>[80]</sup>; g) split-rib resonator (SRR) with an air gap<sup>[81]</sup>; h) chalcogenide MRR for photoacoustic sensing<sup>[91]</sup>; i) waveguide optical cavity ultrasound detector (WOCUD)<sup>[75,163]</sup>; j) silicon BG ultrasound sensor<sup>[83]</sup>; k) polymer inverted-rib waveguide MZI sensor<sup>[74]</sup>; l) membrane-based silicon MZI US.<sup>[120]</sup> Reproduced with permission from refs. [14, 74, 75, 80, 81, 83, 91, 120, 163].

transparent substrate, achieving an axial resolution of 3.57  $\mu\text{m}$  (at best, it can be 2.12  $\mu\text{m}$ <sup>[174]</sup>), as shown in Figure 5e and has been applied to live-mice brain imaging.<sup>[14,124]</sup>

**Si and Si<sub>3</sub>N<sub>4</sub> MRR:** For fine-pitch (2D) arrays with less than 50  $\mu\text{m}$  pitches, polymer MRRs are challenging to achieve small sizes due to low refractive index contrast.<sup>[175]</sup> In contrast, Si/SiN-based MRR USIP detectors are compact and CMOS-compatible, allowing fast mass production for scalable 2D arrays. However, due to the low photoelastic coefficient of Si and silicon nitride (SiN), the typical Si and SiN MRRs exhibit a low sensitivity. Acoustic membranes are usually applied to enhance the ultrasound response of these MRRs. In 2015, Leinders et al. first reported using Si MRRs for ultrasound detection.<sup>[78,176]</sup> Their sensors had a sensitivity of 2.1  $\text{mV}/\text{kPa}$  and NEPD of 0.4  $\text{mPa}/\sqrt{\text{Hz}}$ , and operated with a central frequency of 0.76 MHz. The -6 dB bandwidth was 144.4 KHz and the diameter was 120  $\mu\text{m}$ . Felipe's group later integrated a ring resonator with a fiber MZI system to enhance the detection sensitivity, achieving an intrinsic sensitivity of 21.4  $\text{fm Pa}^{-1}$  and a spatial resolution of 66  $\mu\text{m}$  with their intravascular ultrasound (IVUS) imaging system in 2017.<sup>[121]</sup> The sensors worked at a frequency of  $\approx 1$  MHz. Vladimir Stojanovic's group reported the fabrication of silicon MRRs using a zero-change advanced CMOS-SOI process in 2019, achieving detection at over 10 MHz frequency with a measured Q factor of  $\approx 10^4$ .<sup>[177]</sup> They later fabricated a 4  $\times$  8 MRR sensor array in 2021.<sup>[178,179]</sup> However, their sensors were several hundred microns in size and used individually. In 2022, they integrated an MRR-based ultrasound sensor into a detection system on a single chip.<sup>[180]</sup> In 2020, Yang et al. reported an etched silicon-on-insulator (SOI) MRR ultrasound sensor with an acceptance angle of  $\approx 75$  degrees.<sup>[159]</sup> In addition to Si, devices based on SiN are also CMOS-compatible. In 2019, Robin Singh reported a SiN-

based MRR for photoacoustic sensing working at central frequency 1 MHz with a NEPD < 1  $\text{mPa}/\sqrt{\text{Hz}}$ .<sup>[160]</sup> Though Si and SiN based MRR are CMOS-compatible and small sized, the high Young's modulus and high reflection acoustic loss ( $\approx 6$  dB)<sup>[181]</sup> limit its application in high-frequency ultrasound detection.

According to Equations (23) and (24),  $N \propto Q$ , thus a higher Q factor represses the shot noise, leading to a thermal-noise-dominant  $\text{NEP}_{\text{membrane}}$ . Microdisks (MDs), another whisper-gallery-mode (WGM) resonator, usually have ultra-high Q factors. In 2019, Sahar Basiri-Esfahani reported a silicon MD ultrasound sensor with extremely high sensitivity,<sup>[80]</sup> as shown in Figure 5f. The NEPD of this device is in the range of 8–300  $\mu\text{Pa}/\sqrt{\text{Hz}}$ , with an intrinsic Q of  $3.6 \times 10^6$ . In 2022, Yang et al. reported a MD ultrasound sensor with an optical Q of  $\approx 10^7$ .<sup>[112]</sup> The NEPD is 46  $\mu\text{Pa}/\sqrt{\text{Hz}}$  – 10  $\text{mPa}/\sqrt{\text{Hz}}$  in the frequency range of 0.25–3.2 MHz for acoustic response. And in 2023, they improved the NEPD to be 1.18  $\mu\text{Pa}/\sqrt{\text{Hz}}$ .<sup>[116]</sup> Although their sensitivity is even several orders higher than MRRs, there is a drawback that the best sensitivity only appears in a narrow bandwidth near each mechanical resonance for MD USIP devices.<sup>[80]</sup>

Some researchers have figured out ideas to improve the high-frequency response for Si and SiN MRR by applying micro-mechanical systems or membranes on the MRRs. In 2021, Westerveld et al. induced an air gap membrane over a silicon MRR, as shown in Figure 5g.<sup>[81]</sup> The split-rib resonators (SRR) were reported to have a bandwidth over 30 MHz and an NEPD of 1.3  $\text{mPa}/\sqrt{\text{Hz}}$ . The SRR consists of a silicon MRR, a 15 nm air gap, a silicon slab, and a membrane over it. And the MRR works in TM mode, making it more sensitive for ultrasound. An axial resolution of 20  $\mu\text{m}$  was achieved for a 15  $\mu\text{m}$  MRR. A fine-pitch 2D sensor matrix was also fabricated and coupled through optical

fibers, and the process is COMS-compatible. However, the fabrication process is complicated, significantly increasing the fabrication cost.

**Si or Si<sub>3</sub>N<sub>4</sub> Waveguide Core and Polymer Cladding MRR:** A recent approach to improving the high-frequency response is to coat a soft material (typically a polymer) as the cladding layer and design to have more optical field distribution in the cladding. PDMS is a popular material with Young's modulus of only 1.4 MPa. And the acoustic impedance of PDMS (148 KRayl) is close to water (150 KRayl). According to Eq(9), the  $\alpha_r$  for ultrasound entering PDMS from water is only 0.05 %.<sup>[14]</sup> It was noted that a hybrid structure with a hard core (Si/SiN) and soft polymer cladding enhancing the sensitivity of USIP was first demonstrated by R. Kumar et al. in 2019, though they have not performed it on MRR devices.<sup>[82]</sup> In 2023, Ding et al. added a SU-8 cladding to a TM mode silicon MRR.<sup>[90]</sup> The Si layer is only 220 nm in a standard SOI wafer, whereas TM mode has a larger optical field distribution within the cladding. Thanks to the low Young's modulus and a relatively high Q factor of  $7.4 \times 10^4$ , the NEP of 65 Pa over 20 MHz bandwidth was achieved. And the -6 dB bandwidth was extended to 165 MHz. In 2023, Michael Nagli et al. applied a similar approach. They coated a 400-nm-thickness SiN MRR with PDMS.<sup>[89]</sup> Although the MRR works at TE mode, the thin thickness (400 nm) and narrow width (1  $\mu$ m), together with a low refractive index ( $\approx 2.2$ ), allow a large optical field distribution in PDMS cladding. The 30  $\mu$ m-diameter-SiN MRR has a bandwidth of 120 MHz and NEPD of  $\approx 7 \text{ mPa}/\sqrt{\text{Hz}}$ . However, the narrow width of waveguide limits the Q factor. In 2017, Zhang et al. found out that a slot MRR may show high performance on high-frequency detection by simulation.<sup>[182]</sup> In this approach, the thickness of the cladding layer should be thin enough to avoid the high-frequency absorption attenuation coefficient of PDMS and SU-8. For example, a 10  $\mu$ m PDMS will induce 1.2 dB acoustic attenuation at 100 MHz, which cannot be neglected.<sup>[14]</sup>

**Chalcogenide-Based based MRR:** In 2023, Pan et al. reported a  $1 \times 15$  high Q ( $> 5 \times 10^5$ ) chalcogenide-based MRR ( $r = 20 \mu$ m) array for PACT, demonstrating great potential for chalcogenide MRR ultrasound sensors, as shown in Figure 5h.<sup>[91]</sup> The sensor elements in this array achieved a 6 dB bandwidth of 175 MHz with a NEP of  $2.2 \text{ mPa}/\sqrt{\text{Hz}}$ , and a single bus waveguide was integrated to connect all 15 elements. Chalcogenide glasses (ChGs) show a low Young's modulus (approximately an order of magnitude lower than Si and SiN) and maintain high refractive indices ( $> 2$ ). The example in ref. [91] offers another promising alternative if we can better control the aging of this material. Another innovation is the application of the optical comb system. This application shows another fast PACT implementation for cascading USIP on a single bus waveguide when high Q factors are achieved.

WGM resonators usually have a high Q factor and are small in size. The highest Q factor for WGM resonators reported is  $10^{10}$ ,<sup>[183]</sup> and the smallest one is under submicron level.<sup>[184]</sup> The MRR is considered the ideal structure for USIP based on these two parameters. However, the narrow free spectral range (FSR) for WGM usually appears, and when the diameter goes down, the Q factor falls rapidly. Moreover, when integrated into a matrix, the resonant wavelength control on MRR is relatively imprecise due to small fabrication tolerances on resonant wavelength shifts.

### 3.1.2. Fabry-Perot Resonator Structure

FP resonator is another integrated design for ultrasound sensing. A narrow-linewidth laser beam is utilized to measure the distance between two mirrors forming an F-P resonator, as illustrated in Figure 5b. The characteristic curve of the resonator, represented by the reflected light intensity versus wavelength, exhibits change due to the distance variation between the mirrors. In addition, a soft layer placed on top of the mirrors deflects under pressure to detect acoustic pressure, which alters the distance between the mirrors. As a result, the reflected light intensity changes as a function of the distance between the mirrors shown.

In 2007, Shai Ashkenazi's group reported a 2D sensor array containing gold nanostructure. This device has a 6 dB bandwidth of 57 MHz and works at a central frequency of 40 MHz. They achieved 6 dB axial and lateral resolution of 19 and 38  $\mu$ m, respectively. Moreover, in 2014, this group reported a polymer waveguide FP cavity with two dielectric Bragg mirrors for ultrasound sensing, as shown in Figure 5i.<sup>[75,163]</sup> This device has a bandwidth of 30 MHz and NEP of  $0.03 \text{ Pa}/\sqrt{\text{Hz}}$ .

USIP devices on FP sensors typically have small sensor elements, often at a sub-micron scale, allowing for fine-pitch 2D sensor arrays to be fabricated. However, the detection must be performed under free-space galvo scanning, greatly complicating the PAI system based on waveguide FP-based USIP.

### 3.1.3. Bragg Grating Structure

Next, we introduce USIP devices on BGs, which consist of periodic width gradient waveguides shown in Figure 5c. The periodic waveguide structure forms two BG reflection mirrors. The two mirrors reflect the light to form a standing wave resonant cavity. The resonant wavelength is determined by the period. When acoustic waves are applied to the Bragg grating, they exert pressure and modulate the refractive index, resulting in an effective period modulation. These perturbations ultimately result in resonant wavelength shifting within the device.

In 2012, Shai Ashkenazi's group demonstrated polymer Bragg waveguide ultrasound detectors. They fabricated a  $1 \times 15$  SU-8 device array using direct electron beam lithography, achieving a sensitivity of  $7.6 \text{ pm MPa}^{-1}$ , and an NEP of 5.5 kPa in a bandwidth of 60 MHz. The element is  $500 \times 1.5 \mu$ m.<sup>[102]</sup> In 2014, Vasilis Ntziachristos's group reported an embedded SOI Bragg grating US. In 2014, Vasilis Ntziachristos's group reported an embedded SOI Bragg grating US with a view angle of about 26.6 degrees,<sup>[164]</sup> and in 2020, they reported a sub-micron SOI resonator for photoacoustic/ultrasound sensing, with a 6 dB bandwidth over 230 MHz.<sup>[62,185]</sup> The view angle reached 148 degrees, and the NEPD is  $9 \text{ mPa}/\sqrt{\text{Hz}}$ . The PAM reached a spatial resolution of 0.65  $\mu$ m, the highest resolution of a PAI system based on an integrated photonics platform. This sensor senses the acoustic signal by the side surface, leading to a sub-micro aperture. However, the side surface sensing limits its 2D integration. In 2019, Heming Wei and Sridhar Krishnaswamy reported a direct laser-written  $\pi$ -shift Bragg grating.<sup>[126]</sup> A sensitivity of  $268.4 \text{ mv MPa}^{-1}$  and a Q factor of 18 059 were achieved. A NEP of 5.3 kPa was obtained. Amir Rosenthal's group also contributes

a lot to BG-based ultrasound sensors.<sup>[63,83,86,186]</sup> They first applied the hybrid structure with a hard core (Si/SiN) and soft polymer cladding on a micro resonator by demonstrating a Bragg grating device coated by PDMS with over 200 MHz bandwidth and an NEP of  $2.2 \text{ mPa}/\sqrt{\text{Hz}}$ ,<sup>[83]</sup> shown in Figure 5j. The PACT system reached a resolution of  $25 \mu\text{m}$  for all axes. And they also applied it to mouse ear imaging. Later, they integrated  $5 \times 7 \pi$ -BG (7 on one bus waveguide each) to perform them on PAI.<sup>[127]</sup> In this work, they proposed a femtometer pulse laser method to achieve fast matrix scanning.

USIP devices on BG are manufactured with a CMOS-compatible process and have a highly sensitive sensing area that can be as small as a submicron level, translating to high resolution when used in PAI. The bandwidth of BG-based USIPs is usually over 100 MHz. And the FSR is relatively large and can even be FSR-free.<sup>[154]</sup> A wider FSR can contribute to more element cascading. However, most BG-based USIP devices do not sense the ultrasound by a small aperture, especially when the sensors are integrated into a 2D matrix. The apertures tend to be  $\approx 100 \mu\text{m}$  (except when using facet sensing<sup>[62]</sup>), limiting its acceptance angle. And the Q factor is hard to achieve  $10^4$  level. All BGs applied on USIP use direct coupling, resulting in a high scattering loss on the bus waveguide. A side coupling may be able to decrease this loss and cascade more elements on a single bus waveguide.<sup>[154]</sup>

### 3.2. Non-Resonant Methods

#### 3.2.1. Integrated Mach-Zehnder Interferometer Structure

The USIP device on MZI, illustrated in Figure 5d, detects ultrasound operations based on the optomechanical principle. Ultrasound waves in the appropriate frequency range impinge on the membrane cause excitation in its vibrational mode. This mechanical vibration results in the modulation of the effective length and index of the spiral waveguide, leading to phase modulation of the guided mode. This phase modulation, integrated over the length of the waveguide, leads to modulation of the output power of the MZI. Specifically, the optical power arriving at the combiner MMI is proportional to the effective index and length of the spiral on the membrane. In this manner, the sensor can detect ultrasound waves by measuring the resultant modulation in the output power of the MZI, shown in Figure 3c.

In 2012, Daniel Gallego reported a polymer inverted-rib MZI ultrasound sensor, shown in Figure 5k, with an NEP of  $\approx 102 \text{ Pa}$  for 20 MHz bandwidth,<sup>[74]</sup> whose waveguide is covered with polymer cladding. V. Rochus's group applied their silicon MZI pressure sensor on acoustic sensing working at hundreds of kHz frequency ranges in 2017,<sup>[113]</sup> and in 2020, they applied it to PAI.<sup>[169]</sup> In 2019, Boling Ouyang et al. reported an on-chip MZI US, shown in Figure 5l,<sup>[120]</sup> with a sensitivity of  $0.62 \text{ mV kPa}^{-1}$  and a NEPD of  $0.38 \text{ mPa}/\sqrt{\text{Hz}}$ . The frequency centered at 0.47 MHz and the 6 dB bandwidth is 194.6 kHz. In 2017, Marcel W. Pruessner introduced a micro-/nano-opto-electro-mechanical system (MOEMS/NOEMS) on one arm of the MZI.<sup>[168]</sup> This MZI has a resonance frequency of 2.961 MHz and a mechanical  $Q \approx 10^4$ .

For USIP devices on the MZI platform, the examples previously cited show that the size is typically over  $100 \mu\text{m}$ , which makes it difficult to scale down to a fine-pitch array. Additionally,

**Table 2.** Comparison of PAI systems' parameters based on USIP and traditional platforms.

	Imaging depth [mm]	Depth-to-resolution Ratio (DDR)	Reference
USIP-based			
PAM			
IM-PAM	$\approx 0.025$	$\approx 12$	[173, 185]
SWED-PAM	0.2	44.4	
PACT			
SSR-PACT	10	$\approx 500$	[81, 185]
SWED-PACT	10	1000	
Traditional			
PAM			
SW-PAM	0.1	6.7	[11]
PACT			
3D-PACT	40	108	[153]

the frequency range often centers at sub-MHz levels. The low  $f_c$  and  $FB$  limits its application on PAI.

## 4. Applications of USIP Devices on PAI Systems

Integrated photonics platforms have been employed in several PAI systems, with the key parameters of resolution, imaging depth, imaging speed, and depth-to-resolution ratio (DRR) to be optimized separately.

As shown in Table 2, a DRR of  $\approx 200$  is typical<sup>[187]</sup>; PAM and PACT systems based on USIP devices get a higher DDR factor, implying superior performance. In high-end traditional PACT by L.V. Wang's group,<sup>[153]</sup> the resolution is 0.37-0.39 mm with an imaging depth of 4 cm, a DDR  $\approx 108$ , while for SWED-PACT, the resolution at 1 cm reaches  $10 \mu\text{m}$ , resulting in a DRR of 1000, an order of magnitude higher than the traditional one. And the SSP-PACT resolved  $20 \mu\text{m}$  and a DDR  $\approx 500$  for  $15 \mu\text{m}$  SRR.<sup>[81]</sup> For PAM, PAM in reference [11] showed a DDR  $\approx 12$ , while SWED-PAM shows a resolution of  $4.5 \mu\text{m}$  in an imaging depth of  $200 \mu\text{m}$ , resulting in a DDR of 44.4.

Two methods have been employed for acquiring photoacoustic imaging. The first approach involves scanning individual USIP sensors to capture the imaging, while the second approach utilizes USIP sensor arrays for reconstructing the imaging.

### 4.1. Scanning Methods for Point USIP Sensor Imaging Systems

Most PAI systems utilizing USIP devices employ mechanical scanning, primarily because most USIP devices function as point sensors. Two primary mechanical scanning methods are illustrated in Figure 6. The first method involves fixing the sample on a scanning motor stage (including linear and rotational scanning) for multi-dimensional imaging, as shown in Figure 6a. In contrast, the second utilizes a galvo scanner for scanning the photoacoustic excitation light beam, as shown in Figure 6b. The motor scanning method typically offers a larger field of view (FOV) and greater system robustness.<sup>[64,89,92,185]</sup> However, it is characterized by prolonged scanning time, constraining imaging

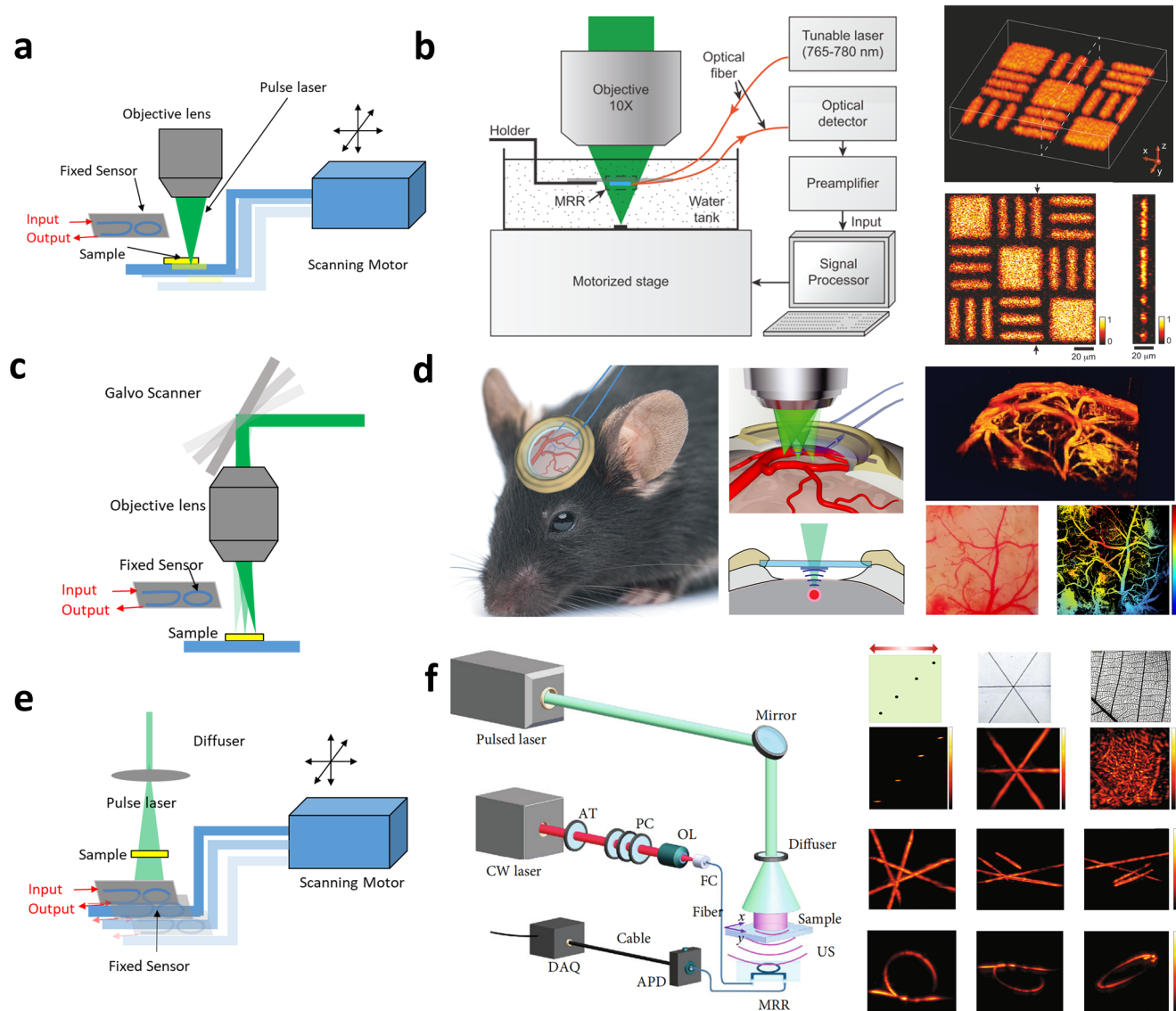


**Figure 6.** Scanning methods and examples of PAI systems using USIP sensors. a) motor scanning PAM system; b) an example of motor scanning PAM<sup>[92]</sup>; c) Galvo scanning PAM; d) an example of galvo scanning PAM<sup>[14]</sup>; e) motor scanning PACT system; f) an example of motor scanning PACT system.<sup>[124]</sup> Reproduced with permission from refs. [14, 92, 124].

efficiency, and limiting the feasibility of 3D real-time imaging. Furthermore, motor scanning may introduce vibrations to the sample, potentially compromising imaging quality. Hao F. Zhang's group first applied this scanning method on a PAM system utilizing USIP devices in 2014.<sup>[64]</sup> The polymer MRRs were integrated on a fiber for endoscopy application, achieving resolutions of 16.0  $\mu\text{m}$  axially, 15.7  $\mu\text{m}$  tangentially, and 4.5  $\mu\text{m}$  radially. Later in the same year, they used an SU-8 MRR, achieving an axial resolution of 5.3  $\mu\text{m}$  and a lateral resolution of 2  $\mu\text{m}$  by mainly improving the acoustic bandwidth of the MRR, shown in Figure 6b.<sup>[92]</sup>

Comparatively, the galvo scanning method demonstrates superior imaging speed owing to the high efficiency of the galvo scanner, making real-time PAI a promising prospect<sup>[14,171,173,174]</sup> This approach avoids introducing vibrations to the sample, rendering

it more suitable for in vivo imaging. However, it is noteworthy that the focusing is not on a flat plane during scanning, leading to potential imaging distortions. Additionally, the scanning area is restricted due to the galvo's limitations in scanning large angles. This method was first applied to USIP-device-based PAM by L. Jay Guo's group in 2011.<sup>[171]</sup> Mouse bladder wall images were obtained with resolutions of 5  $\mu\text{m}$  laterally and 8  $\mu\text{m}$  axially. In 2015, Hao F. Zhang's group also utilized the galvo scanning method, achieving a lateral resolution of 0.72  $\mu\text{m}$  and an axial resolution of 2.12  $\mu\text{m}$ .<sup>[173]</sup> They achieved simultaneous single-cell imaging with extrinsic fluorescence staining, intrinsic autofluorescence, and optical absorption, establishing a foundation for functional biological integrating photoacoustic imaging. In 2019, shown in Figure 6d, they performed in vivo mouse brain imaging with their optimized MRR sensor under galvo scanning PAM, pioneering

an application scenario of integrating photoacoustic imaging for brain research.<sup>[14]</sup>

A modification to the motor scanning PAM system involves replacing the objective lens with a diffuser and fixing the sensor on the motor stage, allowing it to function as a PACT system, as shown in Figure 6e.<sup>[83,89,122,124,172]</sup> Due to challenges in integrating USIP sensor matrices, including fabrication tolerance and readout systems, most PACT systems opt for sensor scanning. Motor-scanning PACT was first performed by L. Jay Guo's Group in 2011, achieving resolutions of 50  $\mu\text{m}$  axially and 55  $\mu\text{m}$  laterally when imaging carbon fibers.<sup>[122]</sup> In 2014, L. Jay Guo's group demonstrated a simple, functional photoacoustic imaging demo of wire and cyst phantoms using 532 and 750 nm lasers.<sup>[172]</sup> In 2022, Junjie Yao's group conducted photoacoustic imaging experiments on ex vivo mouse brain and in vivo mouse ear and tadpole under MRR sensor-based motor scanning PACT system, achieving an imaging depth of 8.5 mm with sub-100-micron resolution, as shown in Figure 6f.<sup>[124]</sup> However, the limitation of this system is that fixed illumination restricts FOV. Notably, in 2023, Amir Rosenthal's group pioneered a technique to scan the illumination with the sensor, thus achieving an unrestricted FOV.<sup>[186]</sup> Although the resolution of PACT can be greatly improved, the imaging time consumption greatly increases. However, the low time consumption is a great advantage of PACT systems compared to PAM systems. A sensor matrix can greatly improve imaging efficiency. Therefore, sensor matrices are the direction of development for USIP sensors.

#### 4.2. USIP Sensor Matrix Imaging System

As universally recognized, US matrices are particularly well-suited for PACT systems, necessitating the development of USIP sensor matrices. While there is a dearth of reports on high-density, large-scale integrated USIP sensor matrices, some researchers have presented notable demonstrations, as depicted in Figure 7.<sup>[73,81,91,127,157,180]</sup>

In 2008, Jay Guo's group pioneered a four-MRR integration on a single waveguide for ultrasound detection.<sup>[73]</sup> Subsequently, in 2021, Westerveld et al. showcased a  $1 \times 10$  sensor matrix demo, with each element functioning independently.<sup>[81]</sup> They asserted its potential for 2D high-density integration, utilizing a continuous-wave (CW) laser tuned to each resonant wavelength to address individual sensor elements, as shown in Figure 7b. Panagiotis Zarkos et al. reported a  $4 \times 8$  sensor matrix in 2023, employing a comb laser for wavelength-division multiplex integration. They achieved resonant wavelength tuning by applying heaters to the MRRs, aligning with the comb laser.<sup>[180]</sup>

An alternative USIP sensor matrix readout approach involves employing a digital frequency comb light source, as illustrated in Figure 7c. The readout principle was initially proposed by Amir Rosenthal in 2014.<sup>[76]</sup> In 2022, Amir's group reported a  $5 \times 7$  sensor matrix based on Bragg Grating sensors.<sup>[127]</sup> However, the sensor could not work simultaneously due to the low Q factor. A low Q resonator matrix integration requires an ultra-broad bandwidth optical modulator for comb laser source generation. In 2023, Pan et al. presented a breakthrough with a  $1 \times 15$  MRR sensor matrix, demonstrating simultaneous operation for each element, facilitated by the high Q factor of the sensor.<sup>[91]</sup> The PACT

systems showed great performance for living zebrafish imaging, as shown in Figure 7d.

The CW-tuning laser method allows large-tolerance sensor fabrication, enabling wafer-scale production in standard foundry manufacturing. However, this approach has inherent drawbacks. Primarily, only one sensor operates at a time with a single detection light, necessitating a corresponding number of lasers for integrated systems, substantially elevating costs. Additionally, the resonant wavelength is susceptible to temperature changes or vibrations, posing challenges related to wavelength mode-lock. These issues may be mitigated by on-chip tunable laser arrays in the future, as depicted in Figure 7e.<sup>[81,157]</sup> On-chip lasers have the potential to significantly reduce costs associated with light power integration and the application of heaters to USIP sensor elements for thermal-optical wavelength tuning.<sup>[180]</sup> Conversely, the frequency-comb readout method has demonstrated successful simultaneous sensor matrix functionality for Photoacoustic Imaging (PAI).<sup>[91]</sup> This approach liberates detection from wavelength-lock constraints and exhibits insensitivity to temperature variations or minor vibrations. However, the low comb tooth spacing restricts the application of high-frequency ultrasound signals in PAI. Moreover, the demanding requirements for a high Q factor, essential for large-scale integration, pose significant reliance on the fabrication process. The future prospect of achieving a THz optical modulator may enhance the performance of frequency-comb readout. As integrated photonics fabrication processes advance, the realization of wafer-scale fabrication for frequency comb readouts becomes a feasible prospect.

#### 5. Prospect and Conclusion

Conventional electrical ultrasound detectors face limitations such as narrow bandwidth, restricted miniaturization, and poor sensitivity. Optical ultrasound detection has shown promise as an alternative due to its superior performance and capabilities, such as high sensitivity and broad bandwidth. Technologies such as free-space optical ultrasound detection have demonstrated improved bandwidth and sensitivity. However, miniaturization is limited due to the long free-space optical path. The measurements are not convenient. Fiber-based ultrasound detection can be fabricated in a high-density 2D sensor array,<sup>[60]</sup> but galvo scanning for element detection limits its efficiency. Moreover, they are challenging to scale up effectively for mass production as USIP devices. CMOS technology facilitates the mass production of USIP devices. USIP devices are usually reported to possess higher sensitivity and broader bandwidth than other optical techniques. Additionally, their compact size allows for a wider acceptance angle. Recent research has also demonstrated the successful integration of USIP devices in 2D fine-pitch arrays.<sup>[81]</sup> As a result of these advantages, USIP is considered one of the most promising techniques for high-resolution ultrasound detection and imaging platforms.

Considering the imaging depth, resolution, and image quality of PAI systems, there are four trends for the future development of USIP and other ultrasound detection methods: high sensitivity, miniaturization, integration, and flexibility. While a flexible USIP has not been demonstrated thus far, its potential to conform to biological tissues and facilitate the fabrication of

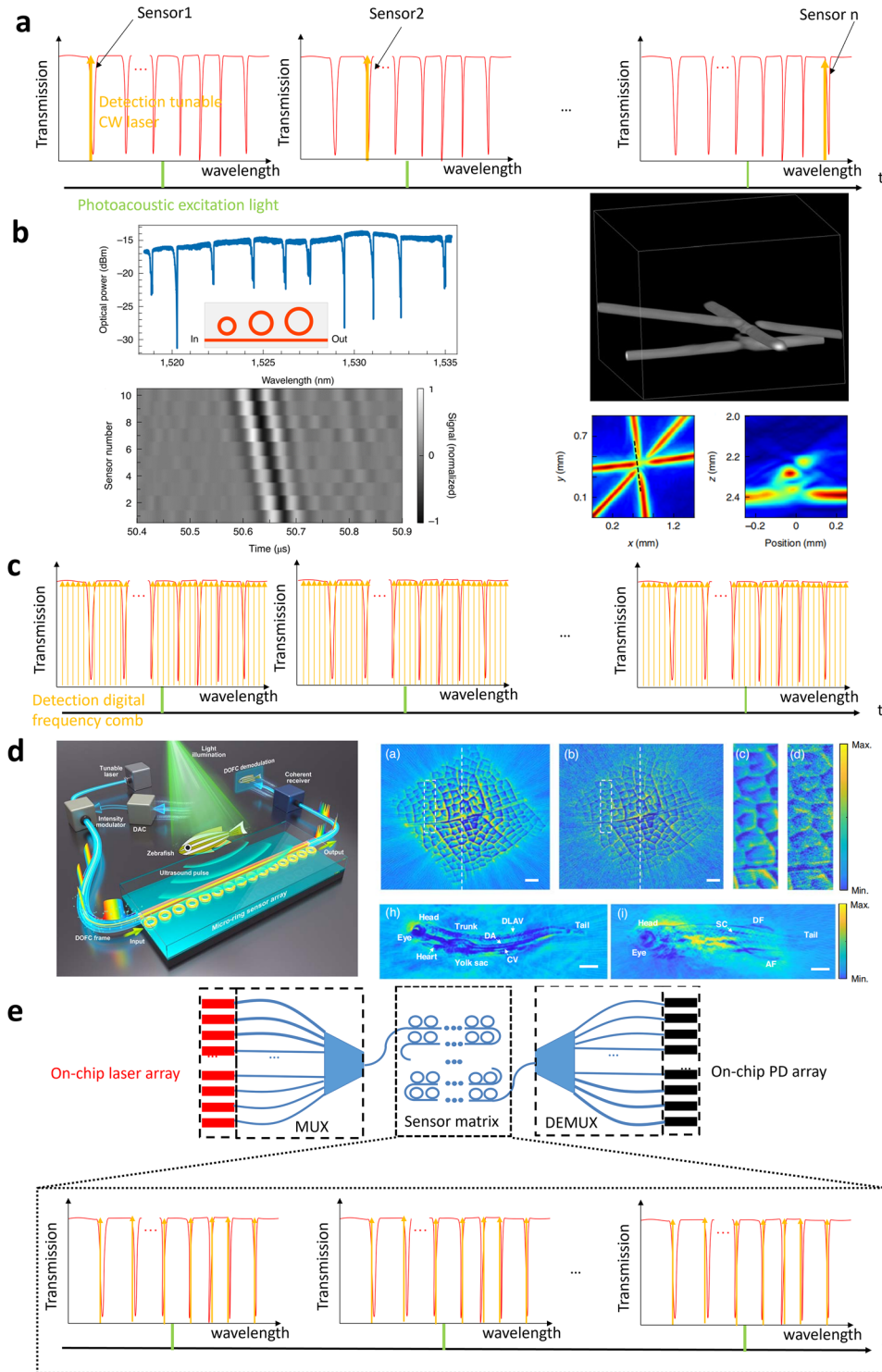


**Figure 7.** USIP Sensor matrix imaging working principle and imaging examples. a) continuous-wave (CW) laser tuning readout; b) an example of CW-laser-readout PACT system<sup>[81]</sup>; c) frequency comb readout; d) an example of frequency-comb-readout PACT system, DOFC: digital optical comb<sup>[91]</sup>; e) Ideal USIP sensor matrix working condition of CW laser tuning readout. MUX: multiplexer; DEMUX: demultiplexer; PD: photodetector. Reproduced with permission from refs. [81, 91].

**Table 3.** Performance comparison of USIP sensors.

Method		NEP(Pa)/NEPD (mPa/√Hz)	$f_c$ (MHz)/FB[%]	Q	Aperture [μm]	Array integration	Fabrication Process	Reference
MRR	Polymer MRR	N.R.	N.R./ N.R.	≈1000	60	Single element	Nanoimprint	[71]
		150k/≈2.4k	40/≈175	600	95	Single element	Nanoimprint	[85]
		230/≈27	≈60/200	6000	100	Single element	Nanoimprint	[87]
		N.R.	N.R./N/R.	N.R.	50	1 × 4	Nanoimprint	[73]
		21.4/≈2.3	38/≈200	4 × 10 <sup>5</sup>	60	Single element	Nanoimprint	[123]
		88/≈10	38/≈200	1.5 × 10 <sup>5</sup>	N.R.	Single element	Nanoimprint	[125]
		29/N.R.	N.R.	3 × 10 <sup>5</sup>	60	Single element	Nanoimprint	[171]
		352/	125/200	4820	60	Single element	EBL	[64]
		N.R.	11.3/154	N.R.	100	Single element	Nanoimprint	[172]
	Si/SiN MRR	0.49/≈0.04	83/200	1.46 × 10 <sup>5</sup>	N.R.	Single element	Nanoimprint	[14]
		0.4/≈1.3	0.76/19	≈ 1.5 × 10 <sup>4</sup>	120	Single element	UP +BDE	[78]
		1.2/N.R.	0.77/14.5	12 706	100	Single element	EBL + BDE	[121]
		N.R.	15/40	≈ 10 <sup>4</sup>	N.R.	Single element	UP	[177]
		N.R./<1	1/N.R.	N.R.	100	Single element	EBL + BDE	[160]
		996/498	> 15/200	≈ 10 <sup>4</sup>	10	4 × 8	UP	[180]
		5.5./1.3	> 15/≈200	18 400	15	1 × 10	EBL + WTWB+ MWE + MuD	[81]
		N.R./0.084	N.R.	3.6 × 10 <sup>6</sup>	≈300	Single element	UP + HF etch	[80]
		N.R./0.046	2.56/≈23	≈10 <sup>7</sup>	57	Single element	UP + MWE	[112]
Polymer coating MRR	65/14.5	82.5/200	7.4 × 10 <sup>4</sup>	20	Single element	EBL	[90]	
	N.R./≈7	75/153	6.1 × 10 <sup>4</sup>	60	Single element	EBL	[89]	
	ChG MRR	7.1/2.2	≈88/≈200	7 × 10 <sup>5</sup>	40	1 × 15	EBL	[91]
FP	N.R.	40/142.5	N.R.	126 × 111	2D high-density	Nanoimprint + LIL	[72]	
	178/30	> 10/≈200	N.R.	20	2D high-density	MuD + EBE + Photolithography	[75]	
BG	Polymer BG	5.5k/≈700	>30/N.R.	N.R.	1.5 × 500	1 × 15	EBL	[102]
		2.93k/N.R.	N.R.	18 059	2 × 100	Single element	DLW	[126]
	Si BG	N.R.	≈20/≈200	≈ 1 × 10 <sup>5</sup>	0.5 × 500	Single element	side corrugation	[164]
		45/9	≈115/≈200	22 232	0.22 × 0.5	1 × 4	UP + a shallow etch + a deep etch + Precision Polish	[62]
	Polymer coating BG	N.R./	>100/≈200	2.2 × 10 <sup>4</sup>	0.5 × 30(TE)	Single element	UP	[83]
		9.8(TE);2.2(TM)	>100/≈200	N.R.	0.5 × 200(TM)			
MZI	Polymer MZI	100/≈22	N.R.	N.R.	N.R.	Single element	Nanoimprint	[74]
	Si MZI	0.38/0.38	0.47/21.2	≈4 × 10 <sup>3</sup>	121 × 121	Single element	UP	[120]
	Polymer coating MZI	N.R.	N.R.	/	N.R.	Single element	N.R.	[82]

EBL: electron beam lithography; BDE: Back deep etch; WTWB: wafer-to-wafer bond; MWE: multiple wet etching; MuD: multiple deposition; UP: ultraviolet-photolithography; LIL: laser interference lithography; EBE: e-beam evaporation; DLW: Direct laser writing; N.R.: Not Reported.

curved surface sensor arrays highlights the significance of achieving flexibility in USIP devices.

We also reviewed four types of USIPs, including MRR, FP, BG, and MZI structures. They can be classified into resonant devices and non-resonant devices. Equations (30) and (31) show the basic optimization directions for a highly sensitive USIP device. As shown in Table 3, MRR-based and BG-based devices show low NEP, broad bandwidth, small aperture, and capability to be integrated into a fine-pitch matrix. However, there are still some chal-

lenges to overcome in both structures. First, the resonant wavelength of the MRR is sensitive to fabrication errors, making matrix scaling difficult. A broad FSR is also required, often resulting in a smaller cavity size. Unfortunately, a smaller size leads to a lower Q factor and decreased sensitivity. On the other hand, BGs offer better control over the resonant wavelength and FSR in the current fabrication process. However, the Q factor is lower compared to MRR devices, with no reported Q factor over 10<sup>5</sup> for fabricated BG USIP devices. Therefore, for MRR USIP devices,

the main challenge is controlling the resonant wavelength, while for BG-based USIP devices, the main challenge lies in achieving a high Q factor.

After analyzing Equation (21) and thoroughly reviewing existing literature on integrated photonics, we believe slot MRRs<sup>[182]</sup> and MRRs with sub-wavelength structures may be an alternative to achieve highly sensitive and broad bandwidth ultrasound detection. In reference,<sup>[188]</sup> the photonic crystal MRR combines an ultra-high Q factor with a large light field distribution in the cladding. When a low Young's modulus material is coated on the MRR, it can potentially become a US detection with high sensitivity. Additionally, the bandgap of the photonic crystals offers a wide free spectral range (FSR) for cascaded sensing units. Furthermore, the position of the defect mode on the transmission spectrum can be more easily controlled compared to an ordinary MRR's resonant wavelength. Besides, strategies to increase the Q factor with high process tolerance are also essential, such as using the gradient width with the MRR to suppress the loss.<sup>[189]</sup>

We confront a significant challenge in the parallel integration of sensor matrices, with two prevailing readout methods for their detection—CW-laser tuning and frequency comb methods. Several sensor matrix demonstrations utilizing these readout approaches have been presented. Consequently, the advancement of USIP technology is on the brink of achieving large-scale integration, wherein all elements operate simultaneously, akin to the functionality exhibited by commercial piezoelectric ultrasound matrices.

In conclusion, there is a growing demand for improving the performance of ultrasound/photoacoustic sensors. Our comparative analysis of these sensors has revealed the significant superiority of USIP over other approaches in terms of resolution, bandwidth, sensitivity, miniaturization, and scalability. We have showcased examples of USIP successfully applied to ultrasound detection and PAI systems. While some aspects of USIP still require further research, we are confident that this emerging technology will contribute to the next-generation photoacoustic/ultrasound sensing, offering substantial benefits to human health.

## Acknowledgements

K.B. and X.Y. contributed equally to this work. This work was supported by the Leading Innovative and Entrepreneur Team Introduction Program of Zhejiang [Grant No. 2020R01005], the "Pioneer" and "Leading Goose" R & D Program of Zhejiang Province [Grant No. 2024SDXHXD0005], the Bright Dream Joint Institute for Intelligent Robotics [Grant No. 10318H991901], National Natural Science Foundation of China [Grant No. 62175202, 12104375, and 62122072], Westlake University [Grant No. 041030080118], the Special Support Plan for Photoelectric Chips Research at Westlake University [Grant No. 10300000H062401/001] and the Key Project of Westlake Institute for Optoelectronics [Grant No. 110500Y0022303].

## Conflict of Interest

The authors declare no conflict of interest.

## Keywords

integrated photonics, optical ultrasound sensor, photoacoustic imaging, ultrasound detection

- [1] A. G. Bell, *J. Soc. Telegraph Eng.* **1880**, 9, 404.
- [2] A. Bychkov, V. Simonova, V. Zarubin, E. Cherepetskaya, A. Karabutov, *Biomed. Ind.: Rev. Appl. Sci-Basel* **2018**, 8, 1931.
- [3] G. Askar'yan, A. Prokhorov, G. Chanturiya, G. Shipulo, *Sov. Phys. JETP* **1963**, 17, 1463.
- [4] R. M. White, *J. Appl. Phys.* **1963**, 34, 3559.
- [5] E. F. Carome, N. A. Clark, C. E. Moeller, *Appl. Phys. Lett.* **1964**, 4, 95.
- [6] S. Cleary, P. Hamrick, *Va. J. Sci* **1968**, 19, 228.
- [7] L. Burmistrova, A. Karabutov, A. Portnyagin, O. Rudenko, E. Cherepetskaya, *Sov. Phys. Acoust* **1978**, 24, 369.
- [8] A. Karabutov, A. Portnyagin, O. Rudenko, E. Cherepetskaya, *Sov. Phys. JETP Lett.* **1979**, 5, 369.
- [9] A. Karabutov, N. Omel'chuk, O. Rudenko, V. Chupryna, *Moscow Univ. Bull. Ser* **1985**, 40, 72.
- [10] L. V. Wang, J. Yao, *Nat. Methods* **2016**, 13, 627.
- [11] C. Zhang, K. Maslov, L. V. Wang, *Opt. Lett.* **2010**, 35, 3195.
- [12] Y. Lee, H. F. Zhang, C. Sun, *Nano Conver.* **2023**, 10, 30.
- [13] M. H. Xu, L. H. V. Wang, *Rev. Sci. Instrum.* **2006**, 77, 041101.
- [14] H. Li, B. Dong, X. Zhang, X. Shu, X. Chen, R. Hai, D. A. Czaplowski, H. F. Zhang, C. Sun, *Nat. Commun.* **2019**, 10, 4277.
- [15] R. Hirayama, D. Martinez Plasencia, N. Masuda, S. Subramanian, *Nature* **2019**, 575, 320.
- [16] *Ultrasound Sensing Technologies 2020*, <https://www.yolegroup.com/product/report/ultrasound-sensing-technologies-2020/>, 2021.
- [17] B. T. Khuri-Yakub, O. Oralkan, *J. Micromech. Microeng.* **2011**, 21, 54004.
- [18] J. M. Rothberg, T. S. Ralston, A. G. Rothberg, J. Martin, J. S. Zahorian, S. A. Alie, N. J. Sanchez, K. Chen, C. Chen, K. Thiele, D. Grosjean, J. Yang, L. Bao, R. Schneider, S. Schaeetz, C. Meyer, A. Neben, B. Ryan, J. R. Petrus, J. Lutsky, D. McMahill, G. Corteville, M. R. Hageman, L. Miller, K. G. Fife, *Proc. Natl. Acad. Sci. USA* **2021**, 118, e2019339118.
- [19] C. Haffner, A. Joerg, M. Doderer, F. Mayor, D. Chelladurai, Y. Fedoryshyn, C. I. Roman, M. Mazur, M. Burla, H. J. Lezec, V. A. Aksyuk, J. Leuthold, *Science* **2019**, 366, 860.
- [20] J. Yao, L. V. Wang, *J. Biomed. Opt.* **2021**, 26, 060602.
- [21] J. P. Monchalain, R. Héon, P. Bouchard, C. Padioleau, *Appl. Phys. Lett.* **1989**, 55, 1612.
- [22] J. D. Hamilton, M. O'Donnell, *IEEE Trans Ultrason Ferroelectr. Freq. Control* **1998**, 45, 216.
- [23] J. Thomson, H. Wickramasinghe, E. Ash, *J. Phys. D: Appl. Phys.* **1973**, 6, 677.
- [24] P. C. Beard, F. Perennes, T. N. Mills, *IEEE Trans. Ultrason. Ferroelectr. Freq. Control* **1999**, 46, 1575.
- [25] B. Fischer, *Nat. Photon.* **2016**, 10, 356.
- [26] C. M. Chow, Y. Zhou, Y. Guo, T. B. Norris, X. Wang, C. X. Deng, J. Y. Ye, *J. Biomed. Opt.* **2011**, 16, 017001.
- [27] K. Pham, S. Noimark, N. Huynh, E. Zhang, F. Kuklis, J. Jaros, A. Desjardins, B. Cox, P. Beard, *IEEE Trans. Ultrason., Ferroelectr. Freq. Control* **2021**, 68, 1007.
- [28] G. Rousseau, B. Gauthier, A. Blouin, J. P. Monchalain, *J. Biomed. Opt.* **2012**, 17, 061217.
- [29] G. Paltauf, H. Schmidt-Kloiber, K. P. Köstli, M. Frenz, *Appl. Phys. Lett.* **1999**, 75, 1048.
- [30] V. V. Yakovlev, W. Dickson, A. Murphy, J. McPhillips, R. J. Pollard, V. A. Podolskiy, A. V. Zayats, *Adv. Mater.* **2013**, 25, 2351.
- [31] J. Boneberg, S. Briaudeau, Z. Demirplak, V. Dobler, P. Leiderer, *Appl. Phys. A: Mater. Sci. Process.* **1999**, 69, S557.
- [32] R. Nuster, G. Paltauf, P. Burgholzer, *Opt. Express* **2007**, 15, 6087.

- [33] A. Schilling, O. Yavaş, J. Bischof, J. Boneberg, P. Leiderer, *Appl. Phys. Lett.* **1996**, *69*, 4159.
- [34] H. Ho, *Opt. Eng.* **2005**, *44*, 124403.
- [35] E. Y. Zhu, C. Rewcastle, R. Gad, L. Qian, O. Levi, *Opt. Lett.* **2019**, *44*, 2609.
- [36] E. Y. Zhu, M. Charles-Herrera, C. Rewcastle, R. Gad, L. Qian, O. Levi, *Opt. Lett.* **2021**, *46*, 3372.
- [37] J. Spytek, L. Ambrozinski, I. Pelivanov, *Photoacoustics* **2023**, *29*, 100440.
- [38] G. Wild, S. Hinckley, *IEEE Sensors J.* **2008**, *8*, 1184.
- [39] W. Heming, G. Zhe, C. Jiawei, P. Fufei, *Laser Optoelectron. Progr.* **2021**, *58*, 1306018.
- [40] R. Chen, G. F. Fernando, T. Butler, R. A. Badcock, *Measur. Sci. Technol.* **2004**, *15*, 1490.
- [41] S. Wang, P. Lu, L. Zhang, D. M. Liu, J. S. Zhang, *IEEE Sensors J.* **2014**, *14*, 2293.
- [42] C. Lan, W. Zhou, Y. Xie, *Sensors* **2018**, *18*, 1218.
- [43] A. J. Prince, F. Kohl, T. Sauter, *Sensors* **2016**, *16*, 1433.
- [44] T. T. Gang, M. L. Hu, X. G. Qiao, J. C. Li, Z. H. Shao, R. X. Tong, Q. Z. Rong, *Opt. Lasers Eng.* **2017**, *88*, 60.
- [45] L. Liu, P. Lu, H. Liao, S. Wang, W. Yang, D. M. Liu, J. S. Zhang, *IEEE Sensors J.* **2016**, *16*, 3054.
- [46] P. A. Fomitchov, S. Krishnaswamy, J. D. Achenbach, *Opt. Eng.* **2000**, *39*, 1972.
- [47] I. Pelivanov, T. Buma, J. Xia, C. W. Wei, M. O'Donnell, *J. Appl. Phys.* **2014**, *115*, 113105.
- [48] L. Wang, N. Fang, C. Wu, H. Qin, Z. Huang, *Sensors* **2014**, *14*, 8398.
- [49] B. Culshaw, *Measur. Sci. Technol.* **2005**, *17*, R1.
- [50] J. Ma, Y. Yu, W. Jin, *Opt. Express* **2015**, *23*, 29268.
- [51] K. Wada, H. Narui, D. Yamamoto, T. Matsuyama, H. Horinaka, *Opt. Express* **2011**, *19*, 21467.
- [52] X. G. Li, L. V. Nguyen, Y. Zhao, H. Eboroff-Heidepriem, S. C. Warren-Smith, *Sensor Actuat B-Chem* **2018**, *269*, 103.
- [53] H. Wei, S. Krishnaswamy, *Appl. Opt.* **2020**, *59*, 530.
- [54] S. V. Thathachary, S. Ashkenazi, *J. Biomed. Opt.* **2018**, *23*, 106008.
- [55] J. A. Guggenheim, J. Li, T. J. Allen, R. J. Colchester, S. Noimark, O. Ogunlade, I. P. Parkin, I. Papakonstantinou, A. E. Desjardins, E. Z. Zhang, P. C. Beard, *Nat. Photon.* **2017**, *11*, 714.
- [56] Q. Rong, R. Zhou, Y. Hao, X. Yin, Z. Shao, T. Gang, X. Qiao, *IEEE Photon. J.* **2017**, *9*, 1.
- [57] H. Wang, Z. W. Xie, M. L. Zhang, H. L. Cui, J. S. He, S. F. Feng, X. K. Wang, W. F. Sun, J. S. Ye, P. Han, Y. Zhang, *Opt. Laser Technol.* **2016**, *78*, 110.
- [58] M. Yao, Y. Zhang, X. Ouyang, A. P. Zhang, H. Y. Tam, P. K. A. Wai, *Opt. Lett.* **2020**, *45*, 3516.
- [59] W. Ni, P. Lu, X. Fu, W. Zhang, P. P. Shum, H. Sun, C. Yang, D. Liu, J. Zhang, *Opt. Express* **2018**, *26*, 20758.
- [60] R. Ansari, E. Z. Zhang, A. E. Desjardins, P. C. Beard, *Light Sci. Appl.* **2018**, *7*, 75.
- [61] B.-O. Guan, L. Jin, J. Ma, Y. Liang, X. Bai, *Opto-Electron. Adv.* **2021**, *4*, 200081.
- [62] R. Shnaiderman, G. Wissmeyer, O. Ulgen, Q. Mustafa, A. Chmyrov, V. Ntziachristos, *Nature* **2020**, *585*, 372.
- [63] M. Nagli, J. Koch, Y. Hazan, A. Levi, O. Ternyak, L. Overmeyer, A. Rosenthal, *Opt. Lett.* **2023**, *48*, 2668.
- [64] B. Dong, S. Chen, Z. Zhang, C. Sun, H. F. Zhang, *Opt. Lett.* **2014**, *39*, 4372.
- [65] L. Wang, Y. Zhao, B. Zheng, Y. Huo, Y. Fan, D. Ma, Y. Gu, P. Wang, *Sci. Adv.* **2023**, *9*, eadg8600.
- [66] Q. Zhang, C. Wu, K. Long, C. Huang, X. Zhong, X. Bai, L. Cheng, L. Jin, Y. Liang, B.-O. Guan, *Opt. Lett.* **2023**, *48*, 1926.
- [67] A. Lula, R. Carotenuto, M. Pappalardo, N. Lamberti, *J. Acoust. Soc. Am.* **2002**, *111*, 2675.
- [68] J. A. Bucaro, H. D. Dardy, E. F. Carome, *Appl. Opt.* **1977**, *16*, 1761.
- [69] Y. Qiu, J. V. Gigliotti, M. Wallace, F. Griggio, C. E. Demore, S. Cochran, S. Trolier-McKinstry, *Sensors* **2015**, *15*, 8020.
- [70] J. F. Dorigi, S. Krishnaswamy, J. D. Achenbach, *IEEE Trans. Ultrason. Ferroelectr., Freq. Control* **1995**, *42*, 820.
- [71] S. Ashkenazi, C.-Y. Chao, L. J. Guo, O'. M. Donnell, *Appl. Phys. Lett.* **2004**, *85*, 5418.
- [72] Y. Hou, J.-S. Kim, S. Ashkenazi, S.-W. Huang, L. J. Guo, O'. M. Donnell, *Appl. Phys. Lett.* **2007**, *91*, 073507.
- [73] A. Maxwell, S. W. Huang, T. Ling, J. S. Kim, S. Ashkenazi, L. J. Guo, *IEEE J. Sel. Top. Quantum Electron.* **2008**, *14*, 191.
- [74] D. Gallego, M. Wang, J. Hiltunen, R. Myllylä, H. Lamela, In *Photons Plus Ultrasound: Imaging and Sensing*, Vol. 8223, SPIE, **2012**.
- [75] M. A. Tadayon, M. E. Baylor, S. Ashkenazi, *IEEE Trans Ultrason Ferroelectr Freq Control* **2014**, *61*, 2132.
- [76] A. Rosenthal, S. Kellnberger, D. Bozhko, A. Chekkoury, M. Omar, D. Razansky, V. Ntziachristos, *Laser Photon. Rev.* **2014**, *8*, 450.
- [77] C. Zhang, T. Ling, S.-L. Chen, L. J. Guo, *ACS Photon.* **2014**, *1*, 1093.
- [78] S. M. Leinders, W. J. Westerveld, J. Pozo, P. L. van Neer, B. Snyder, P. O'Brien, H. P. Urbach, N. de Jong, M. D. Verweij, *Sci. Rep.* **2015**, *5*, 14328.
- [79] Y. Liang, W. Fu, Q. Li, X. Chen, H. Sun, L. Wang, L. Jin, W. Huang, B. O. Guan, *Nat. Commun.* **2022**, *13*, 7604.
- [80] S. Basiri-Esfahani, A. Armin, S. Forstner, W. P. Bowen, *Nat. Commun.* **2019**, *10*, 132.
- [81] W. J. Westerveld, M. Mahmud-Ul-Hasan, R. Shnaiderman, V. Ntziachristos, X. Rottenberg, S. Severi, V. Rochus, *Nat. Photon.* **2021**, *15*, 341.
- [82] R. R. Kumar, E. Hahamovich, S. Tsesses, Y. Hazan, A. Grinberg, A. Rosenthal, *IEEE Photon. J.* **2019**, *11*, 1.
- [83] Y. Hazan, A. Levi, M. Nagli, A. Rosenthal, *Nat. Commun.* **2022**, *13*, 1488.
- [84] J. Yao, L. V. Wang, P. Microscopy, *Laser Photonics Rev.* **2013**, *7*, 758.
- [85] C. Y. Chao, S. Ashkenazi, S. W. Huang, M. O'Donnell, L. J. Guo, *IEEE Trans Ultrason Ferroelectr Freq Control* **2007**, *54*, 957.
- [86] M. Nagli, J. Koch, Y. Hazan, O. Volodarsky, R. Ravi Kumar, A. Levi, E. Hahamovich, O. Ternyak, L. Overmeyer, A. Rosenthal, *Biomed Opt. Express* **2022**, *13*, 6229.
- [87] S. W. Huang, S. L. Chen, T. Ling, A. Maxwell, M. O'Donnell, L. J. Guo, S. Ashkenazi, *Appl. Phys. Lett.* **2008**, *92*, 193509.
- [88] T. Feng, Q. Li, C. Zhang, G. Xu, L. J. Guo, J. Yuan, X. Wang, *Opt. Express* **2016**, *24*, 19853.
- [89] M. Nagli, R. Moisseev, N. Suleymanov, E. Kaminski, Y. Hazan, G. Gelbert, I. Goykhman, A. Rosenthal, *Photoacoustics* **2023**, *32*, 100527.
- [90] Z. Q. Ding, J. L. Sun, C. H. Li, Y. C. Shi, *J. Lightwave Technol.* **2023**, *41*, 1906.
- [91] J. Pan, Q. Li, Y. Feng, R. Zhong, Z. Fu, S. Yang, W. Sun, B. Zhang, Q. Sui, J. Chen, Y. Shen, Z. Li, *Nat. Commun.* **2023**, *14*, 3250.
- [92] H. Li, B. Dong, Z. Zhang, H. F. Zhang, C. Sun, *Sci. Rep.* **2014**, *4*, 4496.
- [93] Z. Zhang, B. Dong, H. Li, F. Zhou, H. F. Zhang, C. Sun, *J. Appl. Phys.* **2014**, *116*, 144501.
- [94] X. Bai, Y. Qi, Y. Liang, J. Ma, L. Jin, B. O. Guan, *Biomed Opt. Express* **2019**, *10*, 2504.
- [95] E. Zhang, J. Laufer, P. Beard, *Appl. Opt.* **2008**, *47*, 561.
- [96] W. Qiao, Z. Chen, W. Zhou, D. Xing, *Opt. Lett.* **2018**, *43*, 2442.
- [97] X. Zhu, Z. Huang, G. Wang, W. Li, D. Zou, C. Li, *Opt. Lett.* **2017**, *42*, 439.
- [98] W. Song, L. Peng, G. Guo, F. Yang, Y. Zhu, C. Zhang, C. Min, H. Fang, S. Zhu, X. Yuan, *ACS Appl. Mater. Interfaces* **2019**, *11*, 27378.
- [99] W. Xia, D. Piras, J. C. van Hespren, S. van Veldhoven, C. Prins, T. G. van Leeuwen, W. Steenbergen, S. Manohar, *Med. Phys.* **2013**, *40*, 032901.

- [100] X. Gao, X. Chen, H. Hu, X. Wang, W. Yue, J. Mu, Z. Lou, R. Zhang, K. Shi, X. Chen, M. Lin, B. Qi, S. Zhou, C. Lu, Y. Gu, X. Yang, H. Ding, Y. Zhu, H. Huang, Y. Ma, M. Li, A. Mishra, J. Wang, S. Xu, *Nat. Commun.* **2022**, *13*, 7757.
- [101] E. Hahamovich, S. Monin, A. Levi, Y. Hazan, A. Rosenthal, *Commun. Eng.* **2022**, *1*, 25.
- [102] V. Govindan, S. Ashkenazi, *IEEE Trans Ultrason Ferroelectr Freq Control* **2012**, *59*, 2304.
- [103] J. Yao, K. I. Maslov, E. R. Puckett, K. J. Rowland, B. W. Warner, L. V. Wang, *Opt. Lett.* **2012**, *37*, 659.
- [104] C. Zhang, K. Maslov, J. Yao, L. V. Wang, *J. Biomed Opt.* **2012**, *17*, 1.
- [105] A. M. Winkler, K. Maslov, L. V. Wang, *J. Biomed Opt.* **2013**, *18*, 097003.
- [106] J. Xia, J. Yao, L. V. Wang, *Electromagn. Waves* **2014**, *147*, 1.
- [107] M. Xu, L. V. Wang, *Phys Rev E Stat Nonlin Soft Matter Phys.* **2003**, *67*, 056605.
- [108] C. Tian, M. Pei, K. Shen, S. Liu, Z. Hu, T. Feng, *Phys. Rev. Appl.* **2020**, *13*, 014001.
- [109] B. Dong, C. Sun, H. F. Zhang, *IEEE Trans. Biomed. Eng.* **2017**, *64*, 4.
- [110] L. H. Edwin, *Geophysics* **1972**, *37*, 620.
- [111] B. E. Treeby, E. Z. Zhang, A. S. Thomas, B. T. Cox, *Ultrasound Med Biol.* **2011**, *37*, 289.
- [112] H. Yang, Z.-G. Hu, Y. Lei, X. Cao, M. Wang, J. Sun, Z. Zuo, C. Li, X. Xu, B.-B. Li, *Phys. Rev. Appl.* **2022**, *18*, 034035.
- [113] V. Rochus, R. Jansen, B. Figeys, F. Verhaegen, R. Rosseel, P. Merken, S. Lenci, X. Rottenberg, *2017 19th Int. Conf. on Solid-State Sensors, Actuators and Microsystems (Transducers)* **2017**, IEEE, pp. 954–957.
- [114] X. Zhou, L. Zhang, W. Pang, *Opt. Express* **2016**, *24*, 18197.
- [115] Y. Lee, Q. Rong, K. H. Song, D. A. Czuplewski, H. F. Zhang, J. Yao, C. Sun, *Photoacoustics* **2023**, *34*, 100574.
- [116] H. Yang, X. Cao, Z.-G. Hu, Y. Gao, Y. Lei, M. Wang, Z. Zuo, X. Xu, B.-B. Li, *Photon. Res.* **2023**, *11*, 1139.
- [117] M. Aspelmeyer, T. J. Kippenberg, F. Marquardt, *Rev. Modern Phys.* **2014**, *86*, 1391.
- [118] H. W. Baac, J. G. Ok, A. Maxwell, K. T. Lee, Y. C. Chen, A. J. Hart, Z. Xu, E. Yoon, L. J. Guo, *Sci. Rep.* **2012**, *2*, 989.
- [119] J. W. Meng, S. J. Tang, J. Sun, K. Shen, C. Li, Q. Gong, Y. F. Xiao, *Phys Rev. Lett.* **2022**, *129*, 073901.
- [120] B. Ouyang, Y. Li, M. Kruidhof, R. Horsten, K. W. A. van Dongen, J. Caro, *Opt. Lett.* **2019**, *44*, 1928.
- [121] F. G. Peternella, B. Ouyang, R. Horsten, M. Haverdings, P. Kat, J. Caro, *Opt. Express* **2017**, *25*, 31622.
- [122] S. L. Chen, T. Ling, L. J. Guo, *J. Biomed. Opt.* **2011**, *16*, 056001.
- [123] T. Ling, S. L. Chen, L. J. Guo, *Appl. Phys. Lett.* **2011**, *98*, 204103.
- [124] Q. Rong, Y. Lee, Y. Tang, T. Vu, C. Taboada, W. Zheng, J. Xia, D. A. Czuplewski, H. F. Zhang, C. Sun, J. Yao, *BME Front* **2022**, *2022*, 1.
- [125] T. Ling, S. L. Chen, L. J. Guo, *Opt. Express* **2011**, *19*, 861.
- [126] H. Wei, S. Krishnaswamy, *Opt. Lett.* **2019**, *44*, 3817.
- [127] Y. Hazan, M. Nagli, A. Levi, A. Rosenthal, *Opt. Lett.* **2022**, *47*, 5660.
- [128] Y. Liang, J. W. Liu, L. Jin, B. O. Guan, L. Wang, *Biomed Opt. Express* **2018**, *9*, 5809.
- [129] A. Rosenthal, D. Razansky, V. Ntziachristos, *Opt. Lett.* **2011**, *36*, 1833.
- [130] G. Rousseau, A. Blouin, J. P. Monchalain, *Biomed. Opt. Express* **2012**, *3*, 16.
- [131] S. Ashkenazi, Y. Hou, T. Buma, O. M. Donnell, *Appl. Phys. Lett.* **2005**, *86*, 134102.
- [132] T. X. Wang, R. Cao, B. Ning, A. J. Dixon, J. A. Hossack, A. L. Klibanov, Q. F. Zhou, A. B. Wang, S. Hu, *Appl. Phys. Lett.* **2015**, *107*, 153702.
- [133] G. Wissmeyer, D. Soliman, R. Shnaiderman, A. Rosenthal, V. Ntziachristos, *Opt. Lett.* **2016**, *41*, 1953.
- [134] Q. Zhou, S. Lau, D. Wu, K. K. Shung, *Prog. Mater. Sci.* **2011**, *56*, 139.
- [135] J. J. Niederhauser, M. Jaeger, M. Hejazi, H. Keppner, M. Frenz, *Opt. Commun.* **2005**, *253*, 401.
- [136] M. Huang, *Int. J. Solids Struct.* **2003**, *40*, 1615.
- [137] M. A. Hopcroft, W. D. Nix, T. W. Kenny, *J. Microelectromech. Syst.* **2010**, *19*, 229.
- [138] T. Capelle, Y. Tsaturyan, A. Barg, A. Schliesser, *Appl. Phys. Lett.* **2017**, *110*, 181106.
- [139] J. Gong, H. Miao, Z. Peng, L. Qi, *Mater. Sci. Eng.: A* **2003**, *354*, 140.
- [140] K. Fujii, T. Noma, O. Masamura, T. Mayama, *JSME Int. J. Series A* **2001**, *44*, 251.
- [141] L. Šimurka, R. Čtvrtilík, J. Tomašík, G. Bektaş, J. Svoboda, K. Bange, *Chem. Pap.* **2018**, *72*, 2143.
- [142] S.-S. Lin, *Ceram. Int.* **2009**, *35*, 2693.
- [143] T. Mahmood, H. Malik, R. Batool, Z. Perveen, F. Saleemi, H. Rasheed, M. A. Saeed, C. Cao, M. Rizwan, *Chin. J. Phys.* **2017**, *55*, 1252.
- [144] L. Li, H. Lin, S. Qiao, Y. Z. Huang, J. Y. Li, J. Michon, T. Gu, C. Alosno-Ramos, L. Vivien, A. Yadav, K. Richardson, N. Lu, J. Hu, *Light Sci. Appl.* **2018**, *7*, 17138.
- [145] I. Papautsky, M. Nordström, W. Wang, D. A. Zauner, A. Boisen, J. Hübner, in *Microfluidics, BioMEMS, and Medical Microsystems IV*, Vol. 6112, SPIE, **2006**.
- [146] S. O. Catarino, G. Minas, J. M. Miranda, *Ultrasonics* **2016**, *69*, 47.
- [147] J. David Musgraves, J. H., L. Calvez, *Handbook of Glass*, Springer, Berlin, Germany **2019**.
- [148] N. Tarjányi, I. Turek, I. Martinček, *Opt. Mater.* **2014**, *37*, 798.
- [149] G. Destgeer, J. H. Jung, J. Park, H. Ahmed, K. Park, R. Ahmad, H. J. Sung, *RSC Adv.* **2017**, *7*, 22524.
- [150] H. Xia, R. Guo, F. Yan, H. Cheng, Z. Lin, Q. Ma, F. Wang, *Optik* **2016**, *127*, 11974.
- [151] S. Hoche, M. A. Hussein, T. Becker, *Ultrasonics* **2015**, *57*, 65.
- [152] V. R. Almeida, M. Lipson, *Opt. Lett.* **2004**, *29*, 2387.
- [153] L. Lin, P. Hu, X. Tong, S. Na, R. Cao, X. Yuan, D. C. Garrett, J. Shi, K. Maslov, L. V. Wang, *Nat. Commun.* **2021**, *12*, 882.
- [154] C. Sun, Y. Yin, Z. Chen, Y. Ye, Y. Luo, H. Ma, L. Wang, M. Wei, J. Jian, R. Tang, H. Dai, J. Wu, J. Li, D. Zhang, H. Lin, L. Li, *PhotonIX* **2022**, *3*, 12.
- [155] C. Sun, C. Zhong, M. Wei, H. Ma, Y. Luo, Z. Chen, R. Tang, J. Jian, H. Lin, L. Li, *Photon. Res.* **2021**, *9*, 1013.
- [156] Y. Luo, C. Sun, M. Wei, H. Ma, Y. Wu, Z. Chen, H. Dai, J. Jian, B. Sun, C. Zhong, J. Li, K. A. Richardson, H. Lin, L. Li, *Nano Lett.* **2023**, *23*, 8898.
- [157] R. Tang, C. Sun, K. Bao, Z. Chen, Z. Ju, M. Wei, Y. Wu, J. Wu, K. Xu, H. Lin, L. Li, *Laser Photon. Rev.* **2023**, *18*, 2300828.
- [158] M. A. A. Caballero, A. Rosenthal, A. Buehler, D. Razansky, V. Ntziachristos, *IEEE Transact. Ultrason., Ferroelectr., Freq. Control* **2013**, *60*, 1234.
- [159] W. Yang, S. Song, K. Powell, X. Tian, L. Li, L. Nguyen, X. Yi, *IEEE Photon. J.* **2020**, *12*, 1.
- [160] R. Singh, A. Agarwal, B. W. Anthony, A. A. Oraevsky, In *Photons Plus Ultrasound: Imaging and Sensing 2020*, Vol. 11240, SPIE, **2020**.
- [161] S. L. Chen, S. W. Huang, T. Ling, S. Ashkenazi, L. J. Guo, *IEEE Trans Ultrason Ferroelectr Freq Control* **2009**, *56*, 2482.
- [162] K. H. Kim, W. Luo, C. Zhang, C. Tian, L. J. Guo, X. Wang, X. Fan, *Sci. Rep.* **2017**, *7*, 109.
- [163] M. A. Tadayan, *Optical Micromachined Ultrasound Transducers (OMUT)—A New Approach for High Frequency Ultrasound Imaging*, Doctoral dissertation, University of Minnesota, **2014**.
- [164] A. Rosenthal, M. Omar, H. Estrada, S. Kellnberger, D. Razansky, V. Ntziachristos, *Appl. Phys. Lett.* **2014**, *104*, 021116.
- [165] Q. Quan, I. B. Burgess, S. K. Tang, D. L. Floyd, M. Loncar, *Opt. Express* **2011**, *19*, 22191.
- [166] Y. Zhao, K. Liu, J. McClelland, M. Lu, *Appl. Phys. Lett.* **2014**, *104*, 161110.
- [167] C. F. Ramirez-Gutierrez, H. D. Martinez-Hernandez, I. A. Lujan-Cabrera, M. E. Rodriguez-Garcia, *Sci. Rep.* **2019**, *9*, 14732.

- [168] M. W. Pruessner, D. A. Kozak, N. A. Tyndall, W. S. Rabinovich, V. Deenadayalan, M. Fanto, S. Preble, T. H. Stievater, *OSA Continuum* **2021**, *4*, 1215.
- [169] M. Zunic, W. J. Westerveld, P. Gijssenbergh, Y. Jeong, A. Miranda, J. O'Callaghan, H. Jafarpoorchekab, E. Vander Poorten, X. Rottenberg, R. Jansen in *2020 21st Int. Conf. on Thermal, Mechanical and Multi-Physics Simulation and Experiments in Microelectronics and Microsystems (EuroSimE)*, IEEE, Piscataway, NJ **2020**, pp 1–8.
- [170] C. Y. Chao, L. J. Guo, *J. Vac. Sci. Technol. B* **2002**, *20*, 2862.
- [171] Z. Xie, S. L. Chen, T. Ling, L. J. Guo, P. L. Carson, X. Wang, *Opt. Express* **2011**, *19*, 9027.
- [172] B. Y. Hsieh, S. L. Chen, T. Ling, L. J. Guo, P. C. Li, *Photoacoustics* **2014**, *2*, 39.
- [173] B. Dong, H. Li, Z. Zhang, K. Zhang, S. Chen, C. Sun, H. F. Zhang, *Optica* **2015**, *2*, 169.
- [174] X. Shu, H. Li, B. Dong, C. Sun, H. F. Zhang, *Biomed Opt. Express* **2017**, *8*, 2851.
- [175] R. Shnaiderman, *Silicon photonics sensors of ultrasound for optoacoustic imaging*, Doctoral dissertation, Technische Universität München, **2021**.
- [176] W. J. Westerveld, *Silicon photonic micro-ring resonators to sense strain and ultrasound*, Delft University of Technology, **2014**.
- [177] P. Zarkos, O. Hsu, V. Stojanović, *CLEO: Science and Innovations*, Optica Publishing Group, **2019**.
- [178] P. Zarkos, S. Buchbinder, C. Adamopoulos, O. Hsu, S. Madhvapathy, J. Whinnery, P. Bhargava, V. Stojanović, *2021 Conference on Lasers and Electro-Optics (CLEO)*, IEEE, **2021**, pp. 1–2.
- [179] P. Zarkos, S. Buchbinder, C. Adamopoulos, S. Madhvapathy, O. Hsu, J. Whinnery, P. Bhargava, V. Stojanovic, in *2021 Symp. on VLSI Circuits*, IEEE, pp. 1–2.
- [180] P. Zarkos, S. Buchbinder, C. Adamopoulos, S. Madhvapathy, O. Hsu, J. Whinnery, P. Bhargava, V. Stojanovic, *IEEE J. Solid-State Circ.* **2022**, *58*, 1.
- [181] J. Carlier, P. Campistron, D. Callens, C. Soyser, B. Nongaillard, S. Wang, X. Zhao, *J. Acoust. Soc. Am.* **2008**, *123*, 3646.
- [182] S. Zhang, J. Chen, S. He, *Opt. Commun.* **2017**, *382*, 113.
- [183] I. S. Grudinin, V. S. Ilchenko, L. Maleki, *Phys. Rev. A* **2006**, *74*, 063806.
- [184] D. Liu, C. Zhang, D. Liang, D. Dai, *Opt. Express* **2019**, *27*, 416.
- [185] R. Shnaiderman, Q. Mustafa, O. Ülgen, G. Wissmeyer, H. Estrada, D. Razansky, A. Chmyrov, V. Ntziachristos, *Adv. Opt. Mater.* **2021**, *9*, 2100256.
- [186] T. Harary, Y. Hazan, A. Rosenthal, *Biomedical Eng. Lett.* **2023**, *13*, 475.
- [187] L. V. Wang, S. Hu, *Science* **2012**, *335*, 1458.
- [188] X. Lu, A. McClung, K. Srinivasan, *Nat. Photon.* **2021**, *16*, 66.
- [189] M. Corato-Zanarella, A. Gil-Molina, X. Ji, M. C. Shin, A. Mohanty, M. Lipson, *Nat. Photon.* **2022**, *17*, 157.



**Kangjian Bao** received his B.S. degree from Zhejiang University in 2021 in Optoelectronic Information Science and Engineering. He has been a Ph.D. Student at Westlake University since August 2021. His research focuses on ultrasound sensing based on integrated photonics.



**Xi Yang** received her B.S. degree in Agricultural Mechanization & Automation and a second B.S. degree in Computer Science & Technology from Shihezi University, Xinjiang, China in 2016. Also, she received a Master's degree in Agricultural Engineering from Shihezi University in 2019. She is pursuing a Ph.D. program in the Center of Excellence in Biomedical Research on Advances-on-Chips Neurotechnologies (CenBRAIN Neurotech) of Westlake University, where she is focusing on non-invasive imaging mainly based on the photoacoustic technique for brain and lungs.



**Chunlei Sun** obtained his B.S. degree (2013) and Ph.D. degree (2019) in the School of Physics and Wuhan National Laboratory for Optoelectronics (WNLO), Huazhong University of Science and Technology (HUST). Then, he was a postdoctoral associate at the School of Engineering, Westlake University for two years. In December 2019, he became an assistant researcher at the School of Engineering, Westlake University. His research focuses on designing and preparing integrated optoelectronic devices and explores optical communication and sensing applications.



**Guoguang Rong** obtained his B.S. degree from Northwestern Polytechnical University (China) in 2000, and M.S. from Rose-Hulman Institute of Technology (USA) in 2003, and Ph.D. from Vanderbilt University (USA) in 2008, all in Electrical Engineering. After getting his Ph.D., Dr. Rong joined Shanghai Jiao Tong University as an Assistant Professor. During 2014-2015, Dr. Rong joined Stanford University as a Visiting Assistant Professor. In 2018, he joined the CenBRAIN Neurotech Center of Excellence of Westlake University as a Research Professor. His research interests are optical biosensors, nanoscale materials and energy devices.



**Chao Tian** is a professor at the School of Engineering Science, University of Science and Technology of China (USTC). He received the B.S. degree in Electrical Engineering and the Ph.D. degree in Optical Engineering from Zhejiang University, Hangzhou, China. From 2013 to 2017, he worked as a Postdoctoral Research Fellow in photoacoustic imaging with the Department of Biomedical Engineering at the University of Michigan, Ann Arbor. He is a Senior Member of SPIE and Optica and a member of IEEE. His research interests focus on photoacoustic and ultrasound imaging and their biomedical applications.



**Junhui Shi** received his PhD at Princeton University. He was working on theoretical chemical dynamics and experimental nuclear magnetic resonance spectroscopy. Afterward, he worked on photoacoustic imaging in the Department of Biomedical Engineering of Washington University in St. Louis, Missouri, and then in the Department of Medical Engineering of Caltech in Pasadena, California. Currently, he is a senior researcher at Zhejiang Lab, Hangzhou, China. His research interests include photoacoustic microscopy, photoacoustic tomography, nuclear magnetic imaging, and their applications in biomedical studies.



**Mohamad Sawan** received the Ph.D. degree in 1990 in Electrical Engineering, from Sherbrooke University, Canada. He is a chair professor, founder, and director of the Center of Excellence in Biomedical Research on Advances-on-Chips Neurotechnologies (CenBRAIN Neurotech) at Westlake University, China. He is an emeritus professor, Polytechnique Montréal, Canada. Dr. Sawan was Editor-in-Chief of the IEEE Transactions on Biomedical Circuits and Systems (2016-2019). He is a Fellow of the Royal Society of Canada, Fellow of the Canadian Academy of Engineering, and Fellow of the IEEE.



**Lan Li** received her B. S. degree in Materials Science and Engineering from the University of Science and Technology of China in 2010, and her Ph.D. degree from the University of Delaware in 2016. She then worked as a postdoctoral associate at the Massachusetts Institute of Technology for three years. In February 2019, she joined Westlake University as an assistant professor. Dr. Li's research interests focus on nanophotonic materials and devices, infrared optical glass materials, integrated flexible photonic device fabrication and characterization, and their explorations for sensing, optogenetics, and bioimaging applications.